THE ASTROPHYSICAL JOURNAL SUPPLEMENT SERIES, 167:315–333, 2006 December
© 2006. The American Astronomical Society. All rights reserved. Printed in U.S.A.

ELECTRON-ION RECOMBINATION RATE COEFFICIENTS AND PHOTOIONIZATION CROSS SECTIONS FOR ASTROPHYSICALLY ABUNDANT ELEMENTS. XII. Na IX, Na X, Mg X, AND Mg XI FOR ULTRAVIOLET AND X-RAY MODELING

SULTANA N. NAHAR
Department of Astronomy, The Ohio State University, Columbus, OH 43210; nahar@astronomy.ohio-state.edu
Received 2006 May 27; accepted 2006 August 16

ABSTRACT

Detailed study on the inverse processes of photoionization and electron-ion recombination for Na IX + $h\nu \leftrightarrow$ Na X + e, Na X + $h\nu \leftrightarrow$ Na XI + e, Mg X + $h\nu \leftrightarrow$ Mg XI + e, and Mg XI + $h\nu \leftrightarrow$ Mg XII + e is reported. The unified method for the total electron-ion recombination is used for the self-consistent results of total and level-specific recombination rate coefficients α_R and $\alpha_R(i)$ (subsuming both radiative recombination [RR] and dielectronic recombination [DR]), total recombination cross sections σ_{RC}, and total and partial level-specific photoionzation cross sections σ_{PI} and $\sigma_{PI}(g)$. The total recombination spectrum of cross sections and recombination rates versus photoelectron energy are presented for experimental applications. The unified method employs close-coupling approximation in the relativistic Breit-Pauli ***R***-matrix (BPRM) method. The coupled channel wave function expansions for Li-like Na IX and Mg X consist of 17 core levels with excitations up to $3d$ orbital and for He-like Na X and Mg XI consist of 16 core levels of excitations up to $4f$ orbital, respectively. The results are presented for all fine-structure levels of the ions up to $n \leq 10$, which correspond to 98 levels with $1/2 \leq J \leq 17/2$ for Li-like Na IX and Mg X, 182 and 185 levels with $0 \leq J \leq 10$ for He-like Na X and Mg XI, respectively. The level specific photoionization cross sections $\sigma_{PI}(nSLJ)$ and recombination rates $\alpha_R(T; nSLJ)$ are obtained for the first time for these ions. The single-valued total $\alpha_R(T)$ is presented over an extended temperature range for astrophysical and laboratory plasma applications. The total unified $\alpha_R(T)$ for all ions agrees very well with the available published RR and DR rates. Total recombination rates for H-like Na XI and Mg XII are also presented for completeness. The results are expected to be accurate within 10%–15% from considerations of important atomic effects such as radiation damping, channel couplings, and interference of DR and RR. The comprehensive data sets are applicable for ionization balance and recombination-cascade models for UV and X-ray lines.

Subject headings: atomic processes — line: formation — X-rays: general

On-line material: machine-readable tables

1. INTRODUCTION

He- and Li-like ions, especially of elements from carbon to iron, are common in X-ray and ultraviolet (UV) emission/absorption of hot astrophysical plasmas and provide powerful diagnostics of physical conditions and chemical composition of the objects (e.g., Hillier 2005). Applications of the atomic parameters for the radiative processes of these ions have been exemplified in earlier works. For example, the distinct spectral Kα lines due to $n = 2$–1 transitions of an He-like ion are widely used for determination of temperature, density, and ionization state of the plasma. Oelgoetz & Pradhan (2001, 2004) employed the unified recombinaton rates to determine the intensity of Kα complex of iron and the ionic abundances of steady and transient astrophysical plasmas. Modeling of recombination-cascade coefficients require level-specific recombination rate coefficients for a large number of excited levels. The unified level specific recombination rate coefficients were used recently to generate the dielectronic satellite line spectra of Fe XXIV and Ni XXVI and identify the satellite lines, especially for the blended lines (Nahar & Pradhan 2006b).

The aim of the present series of papers (e.g., Paper I by Nahar & Pradhan 1997) is to provide accurate parameters for the atomic processes of photoionization and electron-ion recombination for various applications of astrophysical models. He- and Li-like ions have their own characteristic features and require relativistic effects and radiation damping effects to be included for higher resolution and obtain accurate profiles of autoionizing resonances. Detailed and comprehensive studies of level-specific and total photoionization cross sections and recombination rates using the self-consistent unified treatment have been reported for the Li- and He-like ionization stages of various astrophysically abundant elements, C IV, C V (Nahar et al. 2000), O VI, O VII (Nahar & Pradhan 2003), Ne VIII, Ne IX (Nahar & Pradhan 2006a), Fe XXV, Fe XXV (Nahar et al. 2001), Ni XXVI and Ni XXVII (Nahar 2005). N V, N VI, F VIII, and F IX (Nahar 2006). The present report is on Na IX, Na X, Mg XI, and Mg XII. Level-specific recombination rate coefficients, α_i and photoionization cross sections are presented for all levels (n *SLJ*, $n \leq 10$) of each ion. The results should be useful for spectral analysis of X-ray observations from the *Chandra X-ray Observatory* and *XMM-Newton*, UV observations from the *Far Ultraviolet Explorer* (*FUSE*) and other UV satellites such as the *Solar and Heliospheric Observatory* (*SOHO*). The data are presented at all energies and temperatures prevalent in high-temperature sources such as active galactic nuclei, supernova remnants, hot stellar coronae, etc.

2. THEORY

The unified method for total electron-ion recombination (Nahar & Pradhan 1992, 1994) accounts for both radiative and dielectronic recombination processes in an ab initio manner and provides a single set of recombination rate coefficients. Futhermore, it provides self-consistent photoionization and recombination cross sections computed using the same wave function expansion. The present calculations include relativistic fine

structure in the Breit-Pauli ***R***-matrix (BPRM) method as adopted under the Iron Project (IP; Hummer et al. 1993) and the radiation damping of low-lying resonances (Zhang et al. 1999), important for Li- and He-like ions, with highly resolved cross sections.

The two paths for the inverse processes of photoionization and electron-ion recombination are (1) direct photoionization and radiative recombinaton,

$$e + \mathrm{X}^{++} \leftrightarrow h\nu + \mathrm{X}^{+}, \tag{1}$$

and (2) through an intermediate doubly excited autoionizing state as

$$e + \mathrm{X}^{++} \leftrightarrow (\mathrm{X}^{+})^{**} \leftrightarrow \left\{ \begin{matrix} (a)\ e + \mathrm{X}^{++}(\mathrm{AI}) \\ (b)\ h\nu + \mathrm{X}^{+}(\mathrm{DR}) \end{matrix} \right\}, \tag{2}$$

where the autoionizing state leads either to autoionization (AI) or to dielectronic recombination (DR) via radiation damping. RR and DR are inseparable in nature. The unified method subsumes both the RR and DR processes and considers photoionization from and recombination into the infinity of levels of the $(e + \text{ion})$ system in an ab initio manner in the close-coupling (CC) approximation.

In the CC approximation, the recombined ion is represented by the target (core) of N-electron system with the $(N+1)$-th interacting electron. The total wave function, $\Psi(E)$, of the $(N+1)$ electrons ion of symmetry $J\pi$ is an expansion of target eigenfunctions, χ_i, multiplied by the interacting wave function θ as

$$\Psi(\text{ion} + e; E) = A \sum_i \chi_i(\text{ion})\theta_i + \sum_j c_j \Phi_j(\text{ion} + e), \tag{3}$$

where the target is in a specific level $J_i\pi_i$ of the ground or of an excited state and the $(N+1)$-th electron is in a channel, $S_i L_i(J_i)\pi_i k_i^2 \ell_i(J\pi)$, where k_i^2 is its incident kinetic energy. A channel is open or closed depending on positive or negative energy of the electron. The autoionizing resonances result from the couplings of open and closed channels. The Φ_j values are correlation functions of the $(N+1)$ electron system and account for short-range correlations and orthogonality between continuum and bound orbitals.

The relativistic Hamiltonian in the Briet-Pauli ***R***-matrix (BPRM) method is

$$H_{N+1}^{\mathrm{BP}} = H_{N+1}^{\mathrm{NR}} + H_{N+1}^{\mathrm{mass}} + H_{N+1}^{\mathrm{Dar}} + H_{N+1}^{\mathrm{so}}, \tag{4}$$

where the first term, H_{N+1}^{NR}, is the nonrelativistic Hamiltonian, and the additional one-body terms are the mass correction term, H_{N+1}^{mass}, the Darwin term, H_{N+1}^{Dar}, and the spin-orbit interaction term, H_{N+1}^{so} (e.g., Nahar 2005). The set of $SL\pi$ is recoupled for $J\pi$ levels of $(e + \text{ion})$-system, which is followed by diagonalization of the Hamiltonian, $H_{N+1}^{\mathrm{BP}}\Psi = E\Psi$. The positive and negative energies define the continuum ($E = k^2 \geq 0$), Ψ_F, or bound ($E < 0$), Ψ_B, states.

The reduced matrix element for the bound-free transition is $\langle \Psi_B || \boldsymbol{D} || \Psi_F \rangle$, where $\boldsymbol{D}_L = \sum_i r_i$ is the dipole operator in length form, the sum is over the number of electrons. The dipole line strength, $\boldsymbol{S} = |\langle \Psi_B || \boldsymbol{D} || \Psi_F \rangle|^2$, gives the photoionization cross section, $\sigma_{\mathrm{PI}} = [4\pi^2/(3g_i c)]\omega \boldsymbol{S}$, where g_i is the statistical weight factor of the initial bound state and ω is the photon energy.

For H- and He-like recombining ions, the radiative decay rates (A_r) for transitions, $np(^2P^o_{3/2,1/2}) \longrightarrow 1s(^2S_{1/2})$ and $1snp(^1P^o_1) \longrightarrow 1s^2(^1S_0)$, where $n = 2$ and 3, are comparable to those of autoionization (typically $A_a \sim 10^{12}$–10^{14} s^{-1}). Hence, the autoionizing resonances can radiatively damp to a significant extent. The radiative damping effect of all resonances, up to effective quantum number $\nu \leq 10$, of the present ions are considered through a resonance fitting procedure (Sakimoto et al. 1990; Pradhan & Zhang 1997; Zhang et al. 1999).

The photorecombination cross section, σ_{RC}, is obtained from the photoionization cross section, σ_{PI}, through the principle of detailed balance (Milne relation) as

$$\sigma_{\mathrm{RC}}(\epsilon) = \frac{\alpha^2}{4}\frac{g_i}{g_j}\frac{(\epsilon + I)^2}{\epsilon}\sigma_{\mathrm{PI}} \tag{5}$$

in rydberg units; α is the fine-structure constant, ϵ is the photoelectron energy, g_j is the statistical weight factor of the recombined ion, and I is the ionization potential. The quantity σ_{RC} computed from σ_{PI} with sufficiently large number of energies to delineate the nonresonant background and the autoionizing resonances represents both RR and DR processes. Assuming that the recombining ion is in the ground state, the above equation represents the partial photoionization cross sections, leaving the ion in the ground state. Recombination rate coefficients of individual recombined levels are obtained by convolving σ_{RC} over Maxwellian electron distribution $f(v)$ at a given temperature as

$$\alpha_{\mathrm{RC}}(T) = \int_0^\infty v f(v)\sigma_{\mathrm{RC}}\, dv = \frac{4}{\sqrt{2\pi m}}\left(\frac{1}{kT}\right)^{3/2}\int_0^\infty \epsilon e^{-\epsilon/kT}\sigma_{\mathrm{RC}}\, d\epsilon. \tag{6}$$

Contributions from the bound levels are added for the total recombination rate coefficient, α_{RC} and for the total recombination cross sections, σ_{RC}.

The recombination can take place into the ground or any of the excited recombined $(e + \text{ion})$ states. The unified method divides the recombined levels into two groups: group (A) of all possible fine-structure levels of symmetry $J\pi$ with $n \leq n_0$, and group (B) levels with $n_0 < n \leq \infty$. The value of n_0 is typically 10. Individual σ_{PI}, σ_{RC}, and α_R values are obtained for all possible bound levels with $n \leq n_0 \sim 10$ (group A) in the CC approximation as described above.

While recombination in to the levels of group (A) are with principle of detailed balance, group (B) levels, $n_0 < n \leq \infty$, are treated through quantum defect theory of DR within the CC approximation. To each excited threshold of the core, $J_i\pi_i$, belongs a Rydberg series of infinite number of $(N+1)$ electron levels, $J_i\pi_i\nu\ell$, to which recombination can occur. The background contribution from RR of the high ν levels is negligible (except at very low temperature). However, the DR contribution is dominant, especially in the region below the threshold of convergence for high-n resonances. The contributions from these levels are obtained from the DR collision strengths, $\Omega(\mathrm{DR})$, using the extension (Nahar & Pradhan 1994) of radiation damping theory (Bell & Seaton 1985):

$$\Omega(\mathrm{DR}) = \sum_{J\pi}\sum_n (1/2)(2J+1)P_n^{J\pi}(\mathrm{DR}), \tag{7}$$

where the DR probability $P_n^{J\pi}$ in entrance channel n is, $P_n^{J\pi}(\mathrm{DR}) = (1 - \boldsymbol{S}_{e\epsilon}^{\dagger}\boldsymbol{S}_{e\epsilon})_n$, $\boldsymbol{S}_{ee}$ is the matrix for electron scattering *including* radiation damping. The recombination cross section, σ_{RC} in megabarns (Mb), is related to the collision strength, Ω_{RC}, as

$$\sigma_{\mathrm{RC}}(i \rightarrow j)(\mathrm{Mb}) = \pi\Omega_{\mathrm{RC}}(i,j)/(g_i k_i^2)(a_0^2/1 \times 10^{-18}), \tag{8}$$

TABLE 1
TARGET LEVELS IN THE EIGENFUNCTION EXPANSIONS OF Na X, Mg XI, Na XI, AND Mg XII

		E_t (Ry)			E_t (Ry)	
NUMBER	LEVEL	Na X	Mg XI	LEVEL	Na X	Mg XII
1	$1s^2\ ^1S_0$	0.0	0.0	$1s\ ^2S_{1/2}$	0.0	0.0
2	$1s2s\ ^3S_1$	81.3907	97.83487	$2p\ ^2P^o_{1/2}$	90.8669	108.167
3	$1s2p\ ^3P^o_0$	82.1766	98.70835	$2s\ ^2S_{1/2}$	90.8689	108.170
4	$1s2p\ ^3P^o_1$	82.1896	98.71590	$2p\ ^2P^o_{3/2}$	90.9159	108.237
5	$1s2p\ ^3P^o_2$	82.2172	98.74844	$3p\ ^2P^o_{1/2}$	107.711	128.223
6	$1s2s\ ^1S_0$	82.2395	98.77022	$3s\ ^2S_{1/2}$	107.712	128.224
7	$1s2p\ ^1P^o_1$	82.8055	99.38836	$3d\ ^2D_{3/2}$	107.726	128.243
8	$1s3s\ ^3S_1$	96.2408	115.6504	$3p\ ^2P^o_{3/2}$	107.726	128.243
9	$1s3s\ ^1S_0$	96.4603	115.89772	$3d\ ^2D_{5/2}$	107.731	128.250
10	$1s3p\ ^3P^o_2$	96.4705	115.90211	$4p\ ^2P^o_{1/2}$	113.605	135.239
11	$1s3p\ ^3P^o_1$	96.4626	115.89248	$4s\ ^2S_{1/2}$	113.605	135.240
12	$1s3p\ ^3P^o_0$	96.4588	115.89007	$4d\ ^2D_{3/2}$	113.611	135.248
13	$1s3d\ ^3D_1$	96.5905	116.03330	$4p\ ^2P^o_{3/2}$	113.611	135.248
14	$1s3d\ ^3D_2$	96.5915	116.03367	$4f\ ^2F^o_{5/2}$	113.613	135.251
15	$1s3d\ ^3D_3$	96.5941	116.03713	$4d\ ^2D_{5/2}$	113.613	135.251
16	$1s3d\ ^1D_2$	96.5996	116.04347	$4f\ ^2F^o_{7/2}$	113.614	135.252
17	$1s3p\ ^1P^o_1$	96.6379	116.07725			

NOTES.—Na X correlations: $2s^2, 2p^2, 3s^2, 3p^2, 3d^2, 2s2p, 2s3s, 2s3p, 2s3d, 2s4s, 2s4p, 2p3s, 2p3p, 2p3d, 2p4s, 2p4p$. Na X λ_{nl}: 1.1(1*s*), 0.99(2*s*), 1.1(2*p*), 1(3*s*), 1(3*p*), 1(3*d*), 1(4*s*), 1(4*p*).
Mg XI correlations: $2s^2, 2p^2, 3s^2, 3p^2, 3d^2, 2s2p, 2s3s, 2s3p, 2s3d, 2s4s, 2s4p, 2p3s, 2p3p, 2p3d, 2p4s, 2p4p$. Mg XI λ_{nl}: 0.991(1*s*), 0.991(2*s*), 1(2*p*), 1(3*s*), 1(3*p*), 1(3*d*), 1(4*s*), 1(4*p*).

where k_i^2 is in rydberg. Since σ_{RC} diverges at zero-photoelectron energy, the total collision strength, Ω, is used in the recombination rate calculations. It may be noted that the unified method is not restricted to $n = 10$. A detailed calculation of σ_{PI} of high-n levels is unnecessary since they approach hydrogenic behavior. Background photoionization cross sections for the high-n group (B) levels are computed hydrogenically, and the corresponding contribution to α_R is referred to as the "high-n top-up" (Nahar 1996).

The recombination rate coefficient $\alpha_{RC}(E)$ as a function of photoelectron energy E is of interest as it can be measured in the experiment (e.g., Zhang et al. 1999). The value of $\alpha_{RC}(E)$ can be obtained from σ_{RC} as

$$\alpha_{RC}(E) = v\sigma_{RC}(E), \tag{9}$$

where v is the velocity of the photoelectron,

3. COMPUTATIONS

The calculations for photoionization and electron-ion recombination span a number of stages using the BPRM package of codes and several other codes.

The computation is initiated with obtaining the target or core wave function. The BPRM codes (Berrington et al. 1995) begin with the given target wave functions. The atomic structure code SUPERSTUCTURE (Eissner et al. 1974) is used for the target wave function in configuration interaction calculations. The wave function expansions for the Li-like Na IX and Mg X consist of 17 fine-structure levels of the *spectroscopic* configurations $1s^2$, $1s2s$, $1s2p$, $1s3s$, $1s3p$, and $1s3d$ of the core. The levels are presented in Table 1. The set of *correlation* configurations and the Thomas-Fermi scaling parameters for each orbital in the atomic structure calculations are also given in Table 1. The calculated energies are very close to the observed values. However, because of their higher accuracy the observed energies are used in the calculations for more exact position of the resonances. The energies in Table 1 are the observed values from the NIST compilation table.[1]

The second term of the Li-like wave function representing bound state correlation functions includes all possible $(N+1)$ particle configurations from 0 to maximum orbital occupancies of $2s^2$, $2p^2$, $3s^2$, $3p^2$, $3d^2$, $4s$, and $4p$ for both Na IX and Mg X. The radial integrals for the partial wave expansion are specified for $0 \le \ell \le 9$ with a $\boldsymbol{R}$-matrix basis set of 30 continuum functions. Computations are carried out for all angular momenta, $0 \le L \le 11$, $1/2 \le J \le 17/2$.

The coupled channel wave function expansion for the He-like Na X and Mg XI consists of 16 fine-structure levels of the core configurations $1s$, $2s$, $2p$, $3s$, $3p$, $3d$, $4s$, $4p$, $4d$, and $4f$. In the atomic structure calculations, all configurations are treated as spectroscopic and λ is taken to be 1. The energies of the core levels are given in Table 1.

The bound state correlation functions for the He-like Na X and Mg XI included all possible configurations from 0 to maximum orbital occupancies of $1s^2$, $2s^2$, $2p^2$, $3s^2$, $3p^2$, $3d^2$, $4s^2$, $4p^2$, $4d$, and $4f$. The partial wave expansion includes all orbitals $0 \le \ell \le 9$, with an $\boldsymbol{R}$-matrix basis set of 30 continuum functions. Computations are carried out for total angular momenta, $0 \le J \le 10$.

The partial and the total photoionization cross sections are obtained for all bound levels using the BPRM R-matrix codes (Berrington et al. 1995). They are extensions of the Opacity Project codes (Berrington et al. 1987) to include the relativistic effects (Scott & Burke 1980; Scott & Taylor 1982). The energy levels are obtained from STGB and are identified using the code PRCBPID (Nahar & Pradhan 2000). Radiation damping of resonances up to $n = 10$ are included using the extended codes STGF and STGBF (Nahar & Pradhan 1994; Zhang et al. 1999). The narrow resonances of these ions were delineated at a very

[1] NIST compiled database, http://www.nist.gov.

TABLE 2

RADIATIVE DECAY RATES, A_{fi} FOR ALLOWED TRANSITIONS TO THE GROUND LEVEL (GD), $1s^2\ ^1S_0$ FOR Na X, Mg XI AND $1s\ ^2S_{1/2}$ FOR Na XI, Mg XII

Target Level	A_{fi} (s^{-1})
Na X: GD $1s^2\ ^1S_0$	
$1s2p(^3P^o_1)$	1.21E+10
$1s2p(^1P^o_1)$	1.35E+13
$1s3p(^3P^o_1)$	3.55E+09
$1s3p(^1P^o_1)$	3.87E+12
Na XI: GD $1s\ ^2S^{1/2}$	
$2p(^2P^o_{1/2})$	9.16E+12
$2p(^2P^o_{3/2})$	9.16E+12
$3p(^2P^o_{1/2})$	2.42E+12
$3p(^2P^o_{3/2})$	2.43E+12
$4p(^2P^o_{1/2})$	9.61E+11
$4p(^2P^o_{3/2})$	9.72E+11
Mg XI: GD $1s^2\ ^1S_0$	
$1s2p(^3P^o_1)$	2.95E+10
$1s2p(^1P^o_1)$	1.96E+13
$1s3p(^3P^o_1)$	8.74E+09
$1s3p(^1P^o_1)$	5.61E+12
Mg XII: GD $1s\ ^2S^{1/2}$	
$2p(^2P^o_{1/2})$	1.30E+12
$2p(^2P^o_{3/2})$	1.30E+12
$3p(^2P^o_{1/2})$	3.41E+12
$3p(^2P^o_{3/2})$	3.44E+12
$4p(^2P^o_{1/2})$	1.35E+12
$4p(^2P^o_{3/2})$	1.37E+12

fine energy mesh. The program PBPRAD extends the total photoionization cross sections in the high-energy region beyond the highest threshold in target ion by a "tail" using a fitting formula, $\sigma^0_{\rm PI}(E^0/E)^m$, where E^0 is the last tabulated energy beyond the resonances, that is, above all target thresholds and $-1 \geq m \geq -3$, as described in Nahar & Pradhan (1994). For Kramers fit at very high energies, $m = -3$.

The DR collision strengths for the narrow and dense resonances in the energy region, $\nu_0 < \nu \leq \infty$, below each target excited threshold were obtained using STGFDR (Nahar & Pradhan 1994; Zhang et al. 1999). The radiative decay rates for the allowed excited thresholds are given in Table 2.

Level-specific recombination cross sections, $\sigma_{\rm RC}(i)$, into various bound levels $i \equiv n\,(SLJ)$ of the recombined $(e + \text{ion})$ system, are obtained from partial photoionization cross sections $\sigma_{\rm PI}(i, g)$ of the level i using the program RECXS. It sums up the level specific rates and adds with the resonant contributions of high-n ($\nu_0 \leq \nu \leq \infty$) DR for the total recombination rates. As an additional check on the numerical calculations, the total recombination rate coefficients, α_R, are also calculated from the total recombination collision strength, $\Omega_{\rm RC}$, obtained from all the photoionization cross sections, and the DR collision strengths. The difference between the two numerical values is typically a few percent. The background (nonresonant) contribution from the high-n states ($10 < n \leq \infty$) is also included as the "top-up" part (Nahar 1996). This contribution is important at low temperatures where recombination rate is dominated by the RR, but negligible at high temperatures.

4. RESULTS AND DISCUSSION

Results from the detailed study of photoionization and electron-ion recombination of (Na IX $+ h\nu \leftrightarrow$ Na X $+ e$), (Na X $+ h\nu \leftrightarrow$ Na XI $+ e$), (Mg X $+ h\nu \leftrightarrow$ Mg XI $+ e$), and (Mg XI $+ h\nu \leftrightarrow$ Mg XII $+ e$) obtained using the unified method are presented. These include cross sections and recombination rate coefficients for all fine-structure levels up to $n = 10$. Both the *total* photoionization cross section ($\sigma_{\rm PI}$), which includes contributions from channels for ionization into the ground as well as various excited states of the core, and the *partial* cross section, which refers to ionization into the ground state only of the core ion, are presented.

The total recombination rates are presented for a wide range of temperatures. Recombination collision strengths ($\Omega_{\rm RC}$) and cross sections ($\sigma_{\rm RC}$), and velocity-weighted recombination rates as functions of photoelectron energies are illustrated for comparison with laboratory measurements. Some important features in photoionization and electron-ion recombination for individual ions are discussed separately below.

4.1. Na IX *and* Mg X

A total of 98 bound levels with $n \leq 10$, $0 \leq l \leq 9$, $0 \leq L \leq 11$, and total angular momentum $1/2 \leq J \leq 17/2$ are found for Na IX and Mg X (Nahar 2002). The calculated energies agree with the measured values within 1% or less. The present photoionization cross sections and recombination rates for Na IX and Mg X are self-consistent with the oscillator strengths obtained earlier (Nahar 2002) in the BPRM approximation using the same wave function expansion.

4.1.1. *Photoionization*

Total and partial photoionization cross sections are presented for all 98 fine-structure bound levels of Na IX and Mg X. Salient features of some of the levels are illustrated below.

Figures 1 and 2 present photoionization cross section of the ground state ($1s^2\ 2s\ ^2S_{1/2}$) of Na IX and Mg X, respectively. The features in the cross sections are very similar for both the ions. The top panel, (*a*) in each figure, presents the total photoionization cross section, which is the summed over contributions from channels with various target thresholds for ionization, and the bottom panel (*b*) presents the *partial* cross sections for ionization in to the ground $1s^2(^1S_0)$ level of residual ion Na IX and Mg X. The cross section decays smoothly over a large energy region since the first excited levels of $n = 2$ thresholds of the core lie at high energies. The Rydberg series of resonances do not appear for a while. The resonances belonging to the Rydberg series converging on to the $n = 2$ thresholds of the core are high and strong, while those belonging to $n = 3$ levels are much weaker. The initial resonance complexes in the figures are the well known KLL, KLM, etc., complexes belonging to $n = 2$ core thresholds. KLL denotes the series $1s2l2l$, KLM denotes $1s2l3l'$, etc. These resonances contribute to the diagnostic dielectronic satellite lines.

As seen in the figures, the total and the partial cross sections are identical below the first excited level of the residual ion. However, the total $\sigma_{\rm PI}$ is enhanced beyond this threshold by the added contributions from excited channels. The enhancement at the excited $n = 2$ thresholds in the total cross sections is due to the K-shell photoionization:

$$h\nu + (1s^2 2s) \longrightarrow e + (1s2s, 1s2p).$$

One K-shell or $1s$ electron is excited to form an autoionizing state that decays to photoionization as the electron goes to

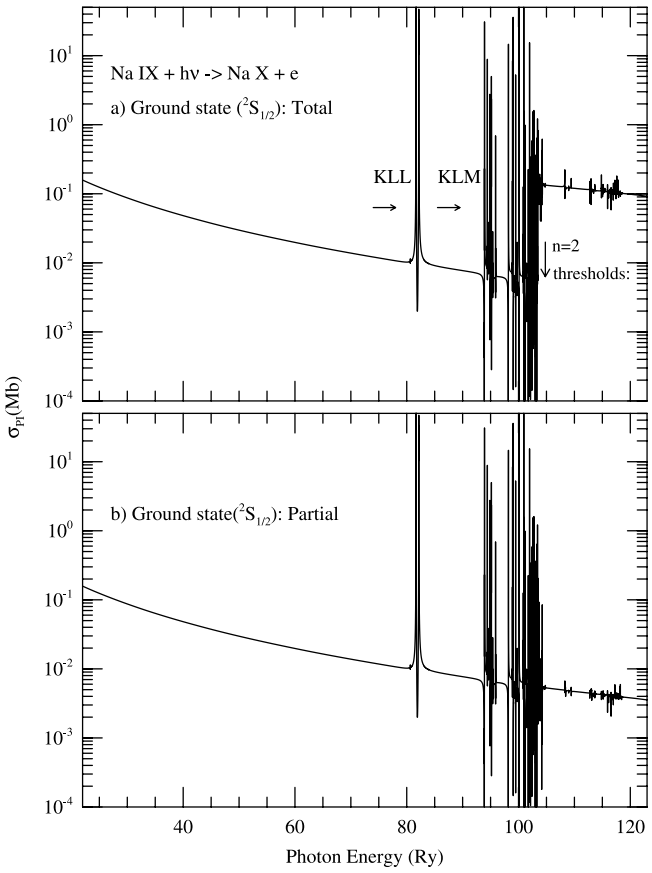

FIG. 1.—Photoionization cross sections ($\sigma_{\rm PI}$) of the ground level $1s^2 2s(^2S_{1/2})$ of Na IX: (*a*) Total cross section; the large jump around $n = 2$ thresholds ($\sim$104.8 ryd) is the K-shell ionization edge ($h\nu + 1s^2 2l \rightarrow 1s2l + e$). (*b*) Partial cross section for ionization into the ground level $1s^2(^1S_0)$ of core Na X; no jump in the partial cross section.

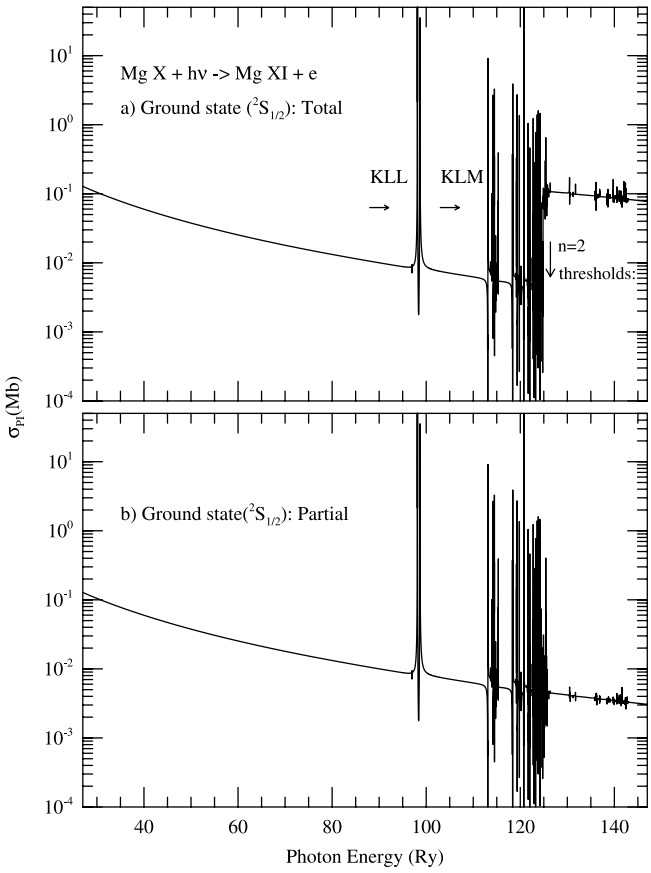

FIG. 2.—Photoionization cross sections ($\sigma_{\rm PI}$) of the ground level $1s^2 2s(^2S_{1/2})$ of Mg X: (*a*) Total cross section; the K-shell ionization jump is around $n = 2$ thresholds ($\sim$126.4 ryd) is due to ($h\nu + 1s^2 2l \rightarrow 1s2l + e$). (*b*) Partial cross section for ionization in to the ground level $1s^2(^1S_0)$ of core Mg XI; no K-shell edge in the partial cross sections.

continuum, The doubly excited autoionizing state is manifested as an enhancement in the photoionzation cross section at the $n = 2$ core threshold. This inner-shell edge plays an important role in X-ray photoionization models.

Figure 3 presents total photoionization cross sections of excited Rydberg series of levels $1s^2 ns(^2S_{1/2})$, $3 \leq n \leq 8$ of Mg X illustrating the resonant structures at higher energies. especially the photoexcitation-of-core (PEC) resonances (Yan & Seaton 1987). The PEC resonances are associated with dipole transitions in the core ion and appear at these excited threshold energies, as shown in the figure by arrows. They are at photon energies of about 99 ryd of $n = 2$ thresholds $1s2p\ ^3P^o_1$, $^1P^o_1$ and about 116 ryd of $n = 3$ thresholds $1s3p\ ^3P^o_1$, $^1P^o_1$ of the core Mg XI. The core goes through the allowed $\Delta J = 0$–1 transitions by absorbing the photon, while the outer electron remains a "spectator" in a doubly excited resonant state. The state autoionizes into the ground level of the core. PEC resonances are much more enhanced than the typical narrow Rydberg resonances and can increase the background cross sections by orders of magnitude. The PEC effect becomes increasingly prominent for cross sections of higher excited levels and exhibit the nonhydrogenic behavior of the cross sections. PEC resonances exist in photoionization cross sections for *all* excited bound levels of Na IX and Mg X.

4.1.2. *Electron-Ion Recombination*

As explained in § 2, the total unified recombination cross sections ($\sigma_{\rm RC}$ and total) unified recombination collision strengths ($\Omega_{\rm RC}$) correspond to summed contributions of photoionization cross sections of all levels. The features of $\Omega_{\rm RC}$ and $\sigma_{\rm RC}$ are similar as they are related through kinematic factors. The unified total $\sigma_{\rm RC}$ for Na IX and Mg X are presented in the top panel of Figures 4 and 5, respectively. The value of $\sigma_{\rm RC}$ diverges at zero photoelectron energy (eq. [8]). It decays smoothly with energy until the emergence of resonance complexes at high energies. A few resonance complexes are marked in the figures: KLL, KLM, KLN, etc., converging onto the $n = 2$ thresholds; and KMM, etc., converging onto the $n = 3$ thresholds. These resonances, especially KLL resonances, manifest themselves as dielectronic satellite lines observed in tokamaks, Electron-Beam-Ion-Traps (EBIT), ion storage rings, and high-temperature astrophysical sources. The unified method has been extended recently to study the prominent KLL satellite lines (Nahar & Pradhan 2006a, 2006b).

The velocity or energy dependent photorecombination rates, $\alpha_{\rm RC}(E)$, for Na IX and Mg X are presented in the bottom panels of Figures 4 and 5. These quantities can be measured in experiments. Hence, the resonant part of $\alpha_{\rm RC}(E)$ converging onto the $n = 2$ threshold, where they are more prominent, of the respective cores are presented for comparison with experiments. However, the measurable feature is the resonant part convolved with the monochromatic bandwidth in the experiment (e.g., as described for C III in Pradhan et al. 2001).

The total recombination rate coefficient $\alpha_{\rm RC}(T)$ for Na IX and Mg X are given for a wide range of temperature. The values are tabulated in Table 3. The main features are illustrated and

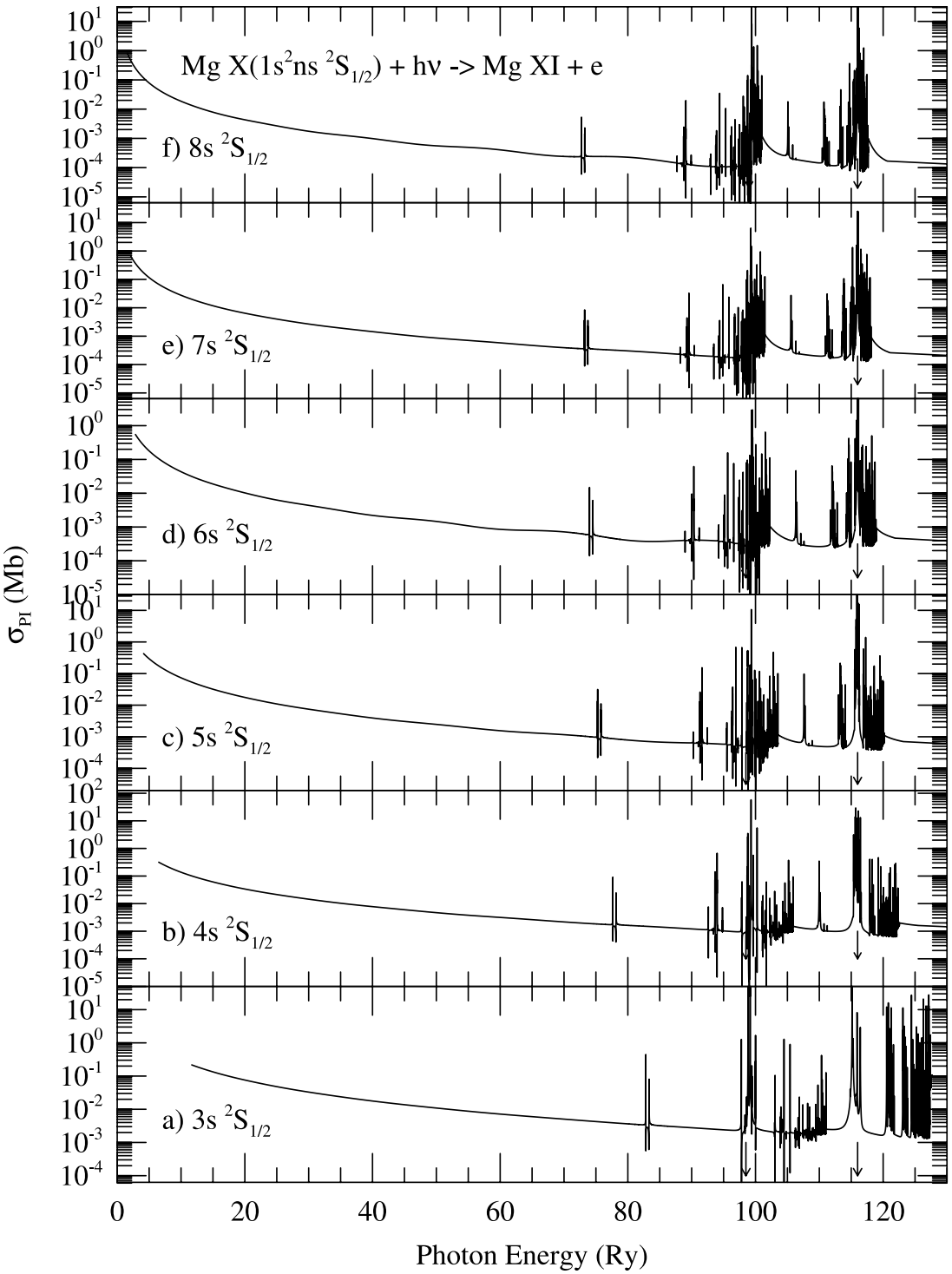

FIG. 3.—Photoionization cross sections of the Rydberg series of levels, $1s^2ns(^2S1/2)$ with $3 \leq n \leq 8$, of Mg x illustrating prominent PEC (*photoexcitation-of-core*) resonances seen (*pointed by arrows*) at about 99 ryd due to excited $n = 2$ core levels $1s2p\ ^3P^o_1$, $^1P^o_1$ and at about 116 ryd due to $n = 3$ core levels $1s3p\ ^3P^o_1$, $^1P^o_1$.

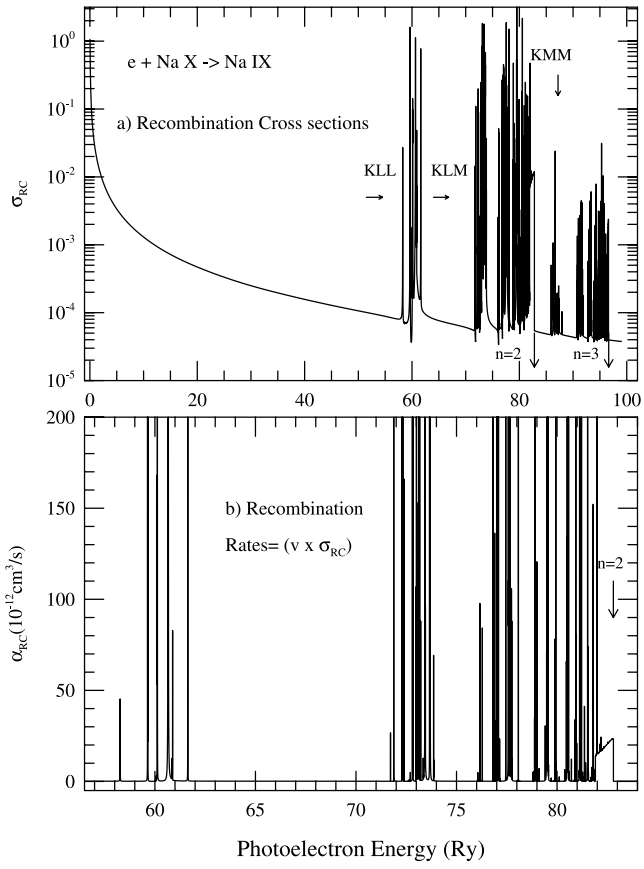

FIG. 4.—(*a*) Total unified (e + ion) recombination cross sections, σ_{RC}, and (*b*) unified recombination rate coefficients, $\alpha_{RC}(E)$, vs. photoelectron energy for (e + Na X → Na IX). Separated resonance complexes, KLL, KLM, etc., of $n = 2$ and KMM, KMN, etc., of $n = 3$ thresholds can be noted. The quantity $\alpha_{RC}(E)$, convolved with an energy bandwidth is measurable.

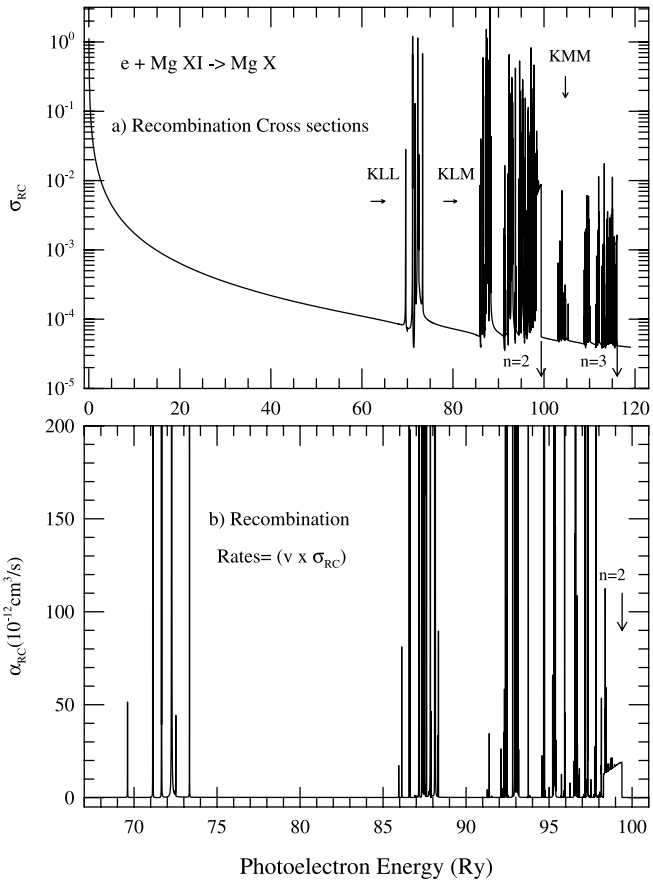

FIG. 5.—(*a*) Total unified (e + ion) recombination cross sections, σ_{RC}, and (*b*) unified recombination rate coefficients, $\alpha_{RC}(E)$, vs. photoelectron energy for (e + Mg IX → Mg X). Separated resonance complexes, KLL, KLM, etc., of $n = 2$ and KMM, KMN, etc., of $n = 3$ thresholds can be noted. The quantity $\alpha_{RC}(E)$, convolved with an energy bandwidth is measurable.

compared with the available data for RR and DR rates in Figures 6*a* and 6*b*. These three-electron atomic systems show the basic features in the total recombination rate coefficient (solid curves) of starting high in the very low temperature, the rate decreases with temperature until at high temperature, where it rises due to dominance of DR to form a DR "bump," which is followed by a monotonic decay. At low temperatures the recombination is via radiative recombination into an infinite number of high-n levels giving smooth decay, and at high temperatures the rise is due to appearance of resonances and the consequent dominance of DR.

The unified total recombination rates are compared with the RR rates by Verner & Ferland (1996) using central field and hydrogenic approximation and DR rates by Romanik (1988) using isolated resonance approximation (IRA). At low T, unified $\alpha_R(T)$ values of both Na IX and Mg X agree very well with the RR rate coefficients (*dashed line*) by Verner & Ferland (1996). At high T where DR contributes dominantly, present rates are compared with those by Romanik, who provides rates for Mg X only. Very good agreement is found between the present rates and those by Romanik (*dot-dashed curve*). This is expected since the interference effect due to RR and DR is small and IRA, which does not consider the background contribution, can provide accurate rates.

Level-specific recombination rate coefficients $\alpha_R(T, i)$ of Na IX and Mg X are presented for all 98 $J\pi$ levels corresponding to $n \leq 10$ and $\ell \leq 9$. Table 4 presents $\alpha_R(T, i)$ into the eight lowest excited $n = 2$ and 3 levels of $n(SLJ)$: $1s^2 2s\ ^2S_0$, $1s^2 2p\ ^2P^o_{1/2,3/2}$, $1s^2 3s\ ^2S_0$, $1s^2 3p\ ^2P^o_{1/2,3/2}$, and $1s^2 3d\ ^2D_{3/2,5/2}$ as often needed for spectral modeling in the UV region. These rates show a smooth feature with a DR "shoulder."

4.2. Na X *and* Mg XI

The total number of fine-structure levels with $n \leq 10$, $0 \leq l \leq 9$, $0 \leq L \leq 14$, and total angular momentum $0 \leq J \leq 10$ obtained for Na IX is 182 and for Mg XI is 185. The calculated energies are in less than 1% in agreement with the observed energies. Photoionization cross sections and recombination rate coefficients are presented for all these levels. The following two subsections describe the important features for photoionization and recombination for these ions.

4.2.1. *Photoionization*

Both partial and total photoionization cross sections are presented for the levels of He-like Na X and Mg XI. Illustrative features in σ_{PI} are shown in Figure 7 for Na X and in Figure 8 for Mg XI. Each figure provides cross sections of the ground level and four diagnostic excited levels corresponding to w, x, y, and z lines for these He-like ions. The features are similar for both the ions. The cross section of all levels for each ion decreases monotonically over a large energy range. As the excited core thresholds lie high in energy, the resonances do not appear for a relatively large energy range.

The top panel of Figures 7 and 8 presents σ_{PI} of the ground level, $1s^2(^1S_0)$ of Na X and Mg XI, respectively. The level shows

TABLE 3

TOTAL RECOMBINATION RATE COEFFICIENTS $\alpha_R(T)$ FOR Na IX–XI, AND Mg X–XII

log T (K)	α_R (cm^3 s^{-1})					
	Na IX	Na X	Na XI	Mg X	Mg XI	Mg XII
1.0	3.31E−09	4.35E−09	5.60E−09	4.11E−09	5.29E−09	6.69E−09
1.1	2.92E−09	3.84E−09	4.96E−09	3.63E−09	4.68E−09	5.93E−09
1.2	2.58E−09	3.40E−09	4.38E−09	3.21E−09	4.14E−09	5.25E−09
1.3	2.27E−09	3.00E−09	3.88E−09	2.83E−09	3.66E−09	4.64E−09
1.4	2.00E−09	2.65E−09	3.43E−09	2.50E−09	3.23E−09	4.10E−09
1.5	1.76E−09	2.33E−09	3.02E−09	2.20E−09	2.85E−09	3.63E−09
1.6	1.55E−09	2.06E−09	2.67E−09	1.94E−09	2.51E−09	3.20E−09
1.7	1.36E−09	1.81E−09	2.35E−09	1.70E−09	2.21E−09	2.82E−09
1.8	1.19E−09	1.59E−09	2.07E−09	1.50E−09	1.95E−09	2.49E−09
1.9	1.05E−09	1.40E−09	1.82E−09	1.31E−09	1.71E−09	2.19E−09
2.0	9.19E−10	1.23E−09	1.60E−09	1.15E−09	1.50E−09	1.92E−09
2.1	8.05E−10	1.08E−09	1.41E−09	1.01E−09	1.32E−09	1.69E−09
2.2	7.03E−10	9.43E−10	1.24E−09	8.83E−10	1.16E−09	1.49E−09
2.3	6.14E−10	8.25E−10	1.08E−09	7.72E−10	1.01E−09	1.30E−09
2.4	5.37E−10	7.22E−10	9.49E−10	6.74E−10	8.87E−10	1.14E−09
2.5	4.68E−10	6.32E−10	8.31E−10	5.89E−10	7.76E−10	1.00E−09
2.6	4.09E−10	5.52E−10	7.28E−10	5.14E−10	6.79E−10	8.78E−10
2.7	3.56E−10	4.82E−10	6.37E−10	4.48E−10	5.93E−10	7.69E−10
2.8	3.10E−10	4.21E−10	5.57E−10	3.91E−10	5.18E−10	6.73E−10
2.9	2.70E−10	3.67E−10	4.87E−10	3.40E−10	4.52E−10	5.88E−10
3.0	2.35E−10	3.20E−10	4.25E−10	2.96E−10	3.94E−10	5.13E−10
3.1	2.04E−10	2.79E−10	3.71E−10	2.57E−10	3.43E−10	4.48E−10
3.2	1.77E−10	2.42E−10	3.24E−10	2.23E−10	2.99E−10	3.91E−10
3.3	1.54E−10	2.11E−10	2.82E−10	1.94E−10	2.60E−10	3.41E−10
3.4	1.33E−10	1.83E−10	2.46E−10	1.68E−10	2.27E−10	2.98E−10
3.5	1.15E−10	1.59E−10	2.14E−10	1.46E−10	1.97E−10	2.60E−10
3.6	9.98E−11	1.38E−10	1.86E−10	1.26E−10	1.71E−10	2.26E−10
3.7	8.63E−11	1.20E−10	1.62E−10	1.09E−10	1.49E−10	1.97E−10
3.8	7.46E−11	1.04E−10	1.41E−10	9.46E−11	1.29E−10	1.71E−10
3.9	6.44E−11	9.02E−11	1.23E−10	8.17E−11	1.12E−10	1.49E−10
4.0	5.55E−11	7.81E−11	1.06E−10	7.05E−11	9.68E−11	1.29E−10
4.1	4.78E−11	6.76E−11	9.25E−11	6.08E−11	8.38E−11	1.12E−10
4.2	4.12E−11	5.84E−11	8.02E−11	5.23E−11	7.25E−11	9.74E−11
4.3	3.54E−11	5.05E−11	6.94E−11	4.51E−11	6.26E−11	8.44E−11
4.4	3.04E−11	4.36E−11	6.03E−11	3.87E−11	5.41E−11	7.32E−11
4.5	2.60E−11	3.76E−11	5.21E−11	3.32E−11	4.67E−11	6.34E−11
4.6	2.23E−11	3.24E−11	4.50E−11	2.85E−11	4.02E−11	5.48E−11
4.7	1.90E−11	2.79E−11	3.89E−11	2.44E−11	3.47E−11	4.74E−11
4.8	1.63E−11	2.40E−11	3.36E−11	2.09E−11	2.98E−11	4.09E−11
4.9	1.39E−11	2.06E−11	2.90E−11	1.78E−11	2.56E−11	3.53E−11
5.0	1.18E−11	1.77E−11	2.49E−11	1.52E−11	2.20E−11	3.05E−11
5.1	1.00E−11	1.51E−11	2.15E−11	1.29E−11	1.89E−11	2.62E−11
5.2	8.48E−12	1.30E−11	1.85E−11	1.09E−11	1.61E−11	2.26E−11
5.3	7.16E−12	1.11E−11	1.58E−11	9.27E−12	1.38E−11	1.94E−11
5.4	6.04E−12	9.46E−12	1.36E−11	7.83E−12	1.18E−11	1.67E−11
5.5	5.08E−12	8.07E−12	1.16E−11	6.60E−12	1.01E−11	1.43E−11
5.6	4.27E−12	6.86E−12	9.96E−12	5.55E−12	8.57E−12	1.22E−11
5.7	3.57E−12	5.83E−12	8.51E−12	4.65E−12	7.29E−12	1.05E−11
5.8	2.98E−12	4.95E−12	7.25E−12	3.89E−12	6.19E−12	8.93E−12
5.9	2.48E−12	4.19E−12	6.18E−12	3.25E−12	5.24E−12	7.61E−12
6.0	2.06E−12	3.53E−12	5.25E−12	2.70E−12	4.43E−12	6.48E−12
6.1	1.71E−12	2.98E−12	4.45E−12	2.24E−12	3.74E−12	5.50E−12
6.2	1.46E−12	2.53E−12	3.77E−12	1.86E−12	3.16E−12	4.66E−12
6.3	1.34E−12	2.18E−12	3.18E−12	1.59E−12	2.68E−12	3.94E−12
6.4	1.40E−12	1.96E−12	2.69E−12	1.42E−12	2.31E−12	3.33E−12
6.5	1.60E−12	1.86E−12	2.25E−12	1.38E−12	2.07E−12	2.81E−12
6.6	1.90E−12	1.84E−12	1.89E−12	1.44E−12	1.93E−12	2.35E−12
6.7	2.17E−12	1.86E−12	1.58E−12	1.54E−12	1.87E−12	1.97E−12
6.8	2.33E−12	1.85E−12	1.31E−12	1.61E−12	1.82E−12	1.64E−12
6.9	2.33E−12	1.77E−12	1.09E−12	1.61E−12	1.75E−12	1.37E−12

TABLE 3—*Continued*

log T (K)	α_R (cm^3 s^{-1})					
	Na IX	Na X	Na XI	Mg X	Mg XI	Mg XII
7.0	2.20E−12	1.64E−12	8.98E−13	1.54E−12	1.63E−12	1.13E−12
7.1	1.96E−12	1.45E−12	7.39E−13	1.39E−12	1.47E−12	9.34E−13
7.2	1.67E−12	1.24E−12	6.04E−13	1.21E−12	1.28E−12	7.68E−13
7.3	1.38E−12	1.03E−12	4.91E−13	1.01E−12	1.08E−12	6.27E−13
7.4	1.10E−12	8.34E−13	3.99E−13	8.20E−13	8.86E−13	5.09E−13
7.5	8.62E−13	6.60E−13	3.20E−13	6.48E−13	7.11E−13	4.12E−13
7.6	6.60E−13	5.14E−13	2.56E−13	5.03E−13	5.60E−13	3.31E−13
7.7	4.99E−13	3.94E−13	2.04E−13	3.83E−13	4.35E−13	2.64E−13
7.8	3.72E−13	2.99E−13	1.61E−13	2.88E−13	3.34E−13	2.10E−13
7.9	2.75E−13	2.25E−13	1.27E−13	2.15E−13	2.53E−13	1.66E−13
8.0	2.02E−13	1.68E−13	9.89E−14	1.59E−13	1.91E−13	1.30E−13
8.1	1.47E−13	1.25E−13	7.69E−14	1.17E−13	1.43E−13	1.01E−13
8.2	1.07E−13	9.27E−14	5.93E−14	8.52E−14	1.07E−13	7.87E−14
8.3	7.70E−14	6.84E−14	4.54E−14	6.19E−14	7.94E−14	6.06E−14
8.4	5.55E−14	5.03E−14	3.48E−14	4.49E−14	5.88E−14	4.64E−14
8.5	3.99E−14	3.69E−14	2.63E−14	3.25E−14	4.35E−14	3.55E−14
8.6	2.86E−14	2.71E−14	1.99E−14	2.34E−14	3.20E−14	2.68E−14
8.7	2.05E−14	1.98E−14	1.50E−14	1.69E−14	2.36E−14	2.03E−14
8.8	1.47E−14	1.45E−14	1.12E−14	1.22E−14	1.73E−14	1.52E−14
8.9	1.05E−14	1.06E−14	8.35E−15	8.74E−15	1.27E−14	1.14E−14
9.0	7.50E−15	7.69E−15	6.19E−15	6.28E−15	9.30E−15	8.47E−15

NOTES.—Table 3 is also available in machine-readable form in the electronic edition of the *Astrophysical Journal Supplement*.

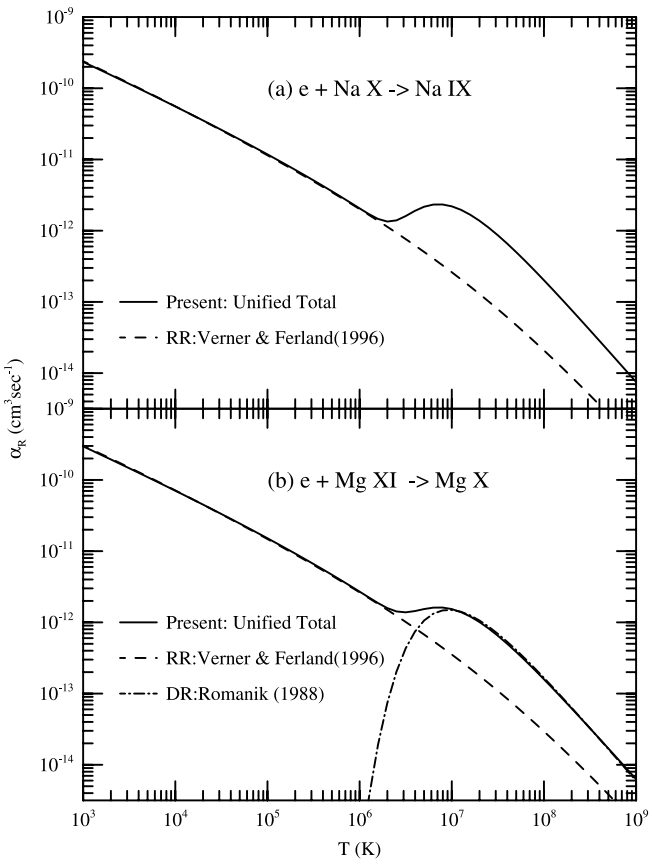

FIG. 6.—Total unified recombination rate coefficients $\alpha_R(T)$ (*solid curves*) for (*a*) Na IX and (*b*) Mg X. The RR rates are by Verner & Ferland (1996, *dashed line*). and the DR rates by Romanik (1988, *dot-dashed line*),

smooth background cross sections with some prominent resonances belonging to $n = 2$ thresholds. The first resonance complex LL ($2l2l$) is easily identifiable in these plots and is followed by Ln' ($n' > 2$) resonances converging on to $n = 2$ thresholds of the core. Beyond $n = 2$ thresholds the resonances are much weaker. There is no jump in the ground state photoionzation cross sections at $n = 2$ thresholds because there is no intermediate state of the two excited electrons.

The bottom four panels present σ_{PI} of the lowest $n = 2$ excited levels corresponding to the prominent X-ray lines of the Kα complex of He-like ions: the resonance line [w: $1s^2(^1S_0) \leftarrow 1s2p(^1P_1^o)$], the intercombination line [y: $1s^2(^1S_0) \leftarrow 1s2p(^3P_1^o)$], and the forbidden lines [x: $1s^2(^1S_0) \leftarrow 1s2p(^3P_2^o)$ and z: $1s^2(^1S_0) \leftarrow 1s2s(^3S_1)$], respectively. In contrast to the ground level, the excited levels show a K-shell jump at the $n = 2$ threshold due to $1s$–$2p$ transition:

$$h\nu + (1s2s, 1s2p) \longrightarrow e + (2s, 2p)$$

as seen in Figures 7*b*–7*e* and 8*b*–8*e*. The transition of $1s$ electron to the excited level forms a doubly excited autoionizing state before decaying to photoionization and introduces the jump at the threshold.

As in the case with Li-like ions, all excited levels of Na X and Mg XI exhibit PEC resonances at the excited core thresholds, allowed to the core ground level.

4.2.2. *Electron-Ion Recombination*

Both the total unified electron-ion recombination collision strength, Ω_{RC}, and the total unified cross section, σ_{RC}, are obtained for the recombined He-like ions, Na X and Mg XI. These two quantities differ by kinematics and hence have similar features. The cross section σ_{RC} for Na X is presented in the top panel of Figure 9 and for Mg XI in Figure 10. Unified σ_{RC} corresponds to the summed contributions of photorecombination cross sections of low-n levels and the DR cross sections of high-n levels. At

TABLE 4

LEVEL SPECIFIC RECOMBINATION RATE COEFFICIENTS FOR THE GROUND AND EXCITED $2l$ AND $3l$ LEVELS OF Na IX AND Mg X

log T (K)	α_R (cm^3 s^{-1})							
	$2s\ ^2S_{1/2}$	$3s\ ^2S_{1/2}$	$2p\ ^2P^o_{1/2}$	$3p\ ^2P^o_{1/2}$	$3d\ ^2D_{3/2}$	$2p\ ^2P^o_{3/2}$	$3p\ ^2P^o_{3/2}$	$3d\ ^2D_{5/2}$
				Na IX				
BE:	−22.0	−9.50	−20.7	−9.14	−9.01	−20.7	−9.14	−9.01
1.0	6.31E−11	1.98E−11	6.27E−11	2.30E−11	3.03E−11	1.25E−10	4.60E−11	4.53E−11
1.1	5.62E−11	1.77E−11	5.59E−11	2.05E−11	2.70E−11	1.11E−10	4.10E−11	4.04E−11
1.2	5.01E−11	1.57E−11	4.98E−11	1.83E−11	2.40E−11	9.91E−11	3.65E−11	3.60E−11
1.3	4.47E−11	1.40E−11	4.44E−11	1.63E−11	2.14E−11	8.83E−11	3.25E−11	3.21E−11
1.4	3.98E−11	1.25E−11	3.96E−11	1.45E−11	1.91E−11	7.87E−11	2.90E−11	2.86E−11
1.5	3.55E−11	1.11E−11	3.53E−11	1.29E−11	1.70E−11	7.02E−11	2.58E−11	2.55E−11
1.6	3.16E−11	9.93E−12	3.14E−11	1.15E−11	1.52E−11	6.25E−11	2.30E−11	2.27E−11
1.7	2.82E−11	8.85E−12	2.80E−11	1.03E−11	1.35E−11	5.57E−11	2.05E−11	2.02E−11
1.8	2.51E−11	7.89E−12	2.50E−11	9.16E−12	1.21E−11	4.97E−11	1.83E−11	1.80E−11
1.9	2.24E−11	7.03E−12	2.22E−11	8.17E−12	1.07E−11	4.43E−11	1.63E−11	1.61E−11
2.0	1.99E−11	6.27E−12	1.98E−11	7.28E−12	9.57E−12	3.95E−11	1.45E−11	1.43E−11
2.1	1.78E−11	5.59E−12	1.77E−11	6.49E−12	8.53E−12	3.52E−11	1.30E−11	1.28E−11
2.2	1.58E−11	4.98E−12	1.57E−11	5.78E−12	7.60E−12	3.13E−11	1.15E−11	1.14E−11
2.3	1.41E−11	4.44E−12	1.40E−11	5.15E−12	6.78E−12	2.79E−11	1.03E−11	1.01E−11
2.4	1.26E−11	3.96E−12	1.25E−11	4.59E−12	6.04E−12	2.49E−11	9.17E−12	9.04E−12
2.5	1.12E−11	3.52E−12	1.11E−11	4.09E−12	5.38E−12	2.22E−11	8.17E−12	8.06E−12
2.6	1.00E−11	3.14E−12	9.93E−12	3.65E−12	4.80E−12	1.98E−11	7.28E−12	7.18E−12
2.7	8.91E−12	2.80E−12	8.85E−12	3.25E−12	4.27E−12	1.76E−11	6.49E−12	6.40E−12
2.8	7.94E−12	2.50E−12	7.89E−12	2.90E−12	3.81E−12	1.57E−11	5.78E−12	5.70E−12
2.9	7.08E−12	2.22E−12	7.03E−12	2.58E−12	3.39E−12	1.40E−11	5.16E−12	5.08E−12
3.0	6.31E−12	1.98E−12	6.27E−12	2.30E−12	3.02E−12	1.25E−11	4.59E−12	4.53E−12
3.1	5.62E−12	1.77E−12	5.59E−12	2.05E−12	2.70E−12	1.11E−11	4.09E−12	4.04E−12
3.2	5.01E−12	1.57E−12	4.98E−12	1.83E−12	2.40E−12	9.91E−12	3.65E−12	3.60E−12
3.3	4.47E−12	1.40E−12	4.44E−12	1.63E−12	2.14E−12	8.83E−12	3.25E−12	3.20E−12
3.4	3.98E−12	1.25E−12	3.95E−12	1.45E−12	1.91E−12	7.87E−12	2.90E−12	2.85E−12
3.5	3.55E−12	1.12E−12	3.52E−12	1.29E−12	1.70E−12	7.01E−12	2.58E−12	2.54E−12
3.6	3.16E−12	9.94E−13	3.14E−12	1.15E−12	1.51E−12	6.25E−12	2.30E−12	2.26E−12
3.7	2.82E−12	8.86E−13	2.80E−12	1.03E−12	1.35E−12	5.57E−12	2.05E−12	2.01E−12
3.8	2.51E−12	7.90E−13	2.49E−12	9.15E−13	1.20E−12	4.96E−12	1.83E−12	1.79E−12
3.9	2.24E−12	7.04E−13	2.22E−12	8.15E−13	1.07E−12	4.42E−12	1.63E−12	1.60E−12
4.0	2.00E−12	6.27E−13	1.98E−12	7.26E−13	9.48E−13	3.94E−12	1.45E−12	1.42E−12
4.1	1.78E−12	5.59E−13	1.76E−12	6.47E−13	8.43E−13	3.50E−12	1.29E−12	1.26E−12
4.2	1.59E−12	4.99E−13	1.57E−12	5.76E−13	7.49E−13	3.12E−12	1.15E−12	1.12E−12
4.3	1.41E−12	4.45E−13	1.40E−12	5.13E−13	6.65E−13	2.78E−12	1.02E−12	9.95E−13
4.4	1.26E−12	3.96E−13	1.24E−12	4.57E−13	5.89E−13	2.47E−12	9.11E−13	8.83E−13
4.5	1.12E−12	3.54E−13	1.10E−12	4.06E−13	5.22E−13	2.20E−12	8.11E−13	7.82E−13
4.6	1.00E−12	3.15E−13	9.82E−13	3.61E−13	4.62E−13	1.96E−12	7.21E−13	6.91E−13
4.7	8.93E−13	2.81E−13	8.73E−13	3.21E−13	4.08E−13	1.74E−12	6.41E−13	6.10E−13
4.8	7.96E−13	2.51E−13	7.75E−13	2.85E−13	3.59E−13	1.54E−12	5.69E−13	5.37E−13
4.9	7.10E−13	2.24E−13	6.87E−13	2.53E−13	3.15E−13	1.37E−12	5.05E−13	4.72E−13
5.0	6.33E−13	2.00E−13	6.09E−13	2.25E−13	2.76E−13	1.21E−12	4.48E−13	4.13E−13
5.1	5.65E−13	1.78E−13	5.39E−13	1.99E−13	2.41E−13	1.07E−12	3.97E−13	3.60E−13
5.2	5.04E−13	1.59E−13	4.76E−13	1.76E−13	2.09E−13	9.48E−13	3.51E−13	3.13E−13
5.3	4.50E−13	1.42E−13	4.20E−13	1.55E−13	1.80E−13	8.35E−13	3.09E−13	2.70E−13
5.4	4.01E−13	1.27E−13	3.69E−13	1.36E−13	1.55E−13	7.35E−13	2.72E−13	2.32E−13
5.5	3.58E−13	1.13E−13	3.24E−13	1.20E−13	1.32E−13	6.44E−13	2.38E−13	1.98E−13
5.6	3.20E−13	1.01E−13	2.83E−13	1.04E−13	1.12E−13	5.63E−13	2.08E−13	1.67E−13
5.7	2.85E−13	9.01E−14	2.46E−13	9.09E−14	9.37E−14	4.89E−13	1.81E−13	1.40E−13
5.8	2.55E−13	8.03E−14	2.13E−13	7.88E−14	7.79E−14	4.24E−13	1.57E−13	1.17E−13
5.9	2.27E−13	7.15E−14	1.84E−13	6.79E−14	6.42E−14	3.65E−13	1.35E−13	9.61E−14
6.0	2.03E−13	6.37E−14	1.57E−13	5.81E−14	5.24E−14	3.13E−13	1.16E−13	7.85E−14
6.1	1.83E−13	5.72E−14	1.35E−13	4.96E−14	4.24E−14	2.69E−13	9.92E−14	6.37E−14
6.2	1.71E−13	5.34E−14	1.20E−13	4.27E−14	3.45E−14	2.37E−13	8.65E−14	5.27E−14
6.3	1.69E−13	5.47E−14	1.12E−13	3.80E−14	2.89E−14	2.21E−13	8.07E−14	4.68E−14
6.4	1.79E−13	6.34E−14	1.13E−13	3.63E−14	2.62E−14	2.22E−13	8.38E−14	4.72E−14
6.5	1.97E−13	7.88E−14	1.19E−13	3.73E−14	2.59E−14	2.35E−13	9.54E−14	5.35E−14
6.6	2.16E−13	9.68E−14	1.27E−13	3.98E−14	2.71E−14	2.49E−13	1.11E−13	6.29E−14
6.7	2.29E−13	1.12E−13	1.32E−13	4.20E−14	2.85E−14	2.57E−13	1.24E−13	7.14E−14
6.8	2.30E−13	1.20E−13	1.30E−13	4.26E−14	2.89E−14	2.53E−13	1.31E−13	7.61E−14
6.9	2.19E−13	1.20E−13	1.22E−13	4.11E−14	2.79E−14	2.36E−13	1.30E−13	7.58E−14

TABLE 4—*Continued*

log T (K)	α_R (cm^3 s^{-1})							
	$2s\ ^2S_{1/2}$	$3s\ ^2S_{1/2}$	$2p\ ^2P^o_{1/2}$	$3p\ ^2P^o_{1/2}$	$3d\ ^2D_{3/2}$	$2p\ ^2P^o_{3/2}$	$3p\ ^2P^o_{3/2}$	$3d\ ^2D_{5/2}$
				Na IX				
7.0	1.98E−13	1.12E−13	1.09E−13	3.76E−14	2.56E−14	2.11E−13	1.21E−13	7.09E−14
7.1	1.73E−13	1.00E−13	9.34E−14	3.29E−14	2.24E−14	1.80E−13	1.07E−13	6.28E−14
7.2	1.45E−13	8.51E−14	7.73E−14	2.77E−14	1.89E−14	1.49E−13	9.03E−14	5.33E−14
7.3	1.18E−13	7.00E−14	6.21E−14	2.26E−14	1.54E−14	1.20E−13	7.39E−14	4.36E−14
7.4	9.42E−14	5.59E−14	4.88E−14	1.79E−14	1.22E−14	9.39E−14	5.87E−14	3.47E−14
7.5	7.37E−14	4.37E−14	3.76E−14	1.39E−14	9.42E−15	7.23E−14	4.57E−14	2.69E−14
7.6	5.68E−14	3.35E−14	2.85E−14	1.06E−14	7.17E−15	5.49E−14	3.49E−14	2.05E−14
7.7	4.32E−14	2.54E−14	2.14E−14	8.02E−15	5.38E−15	4.11E−14	2.62E−14	1.54E−14
7.8	3.26E−14	1.90E−14	1.59E−14	5.97E−15	3.99E−15	3.05E−14	1.95E−14	1.14E−14
7.9	2.44E−14	1.41E−14	1.17E−14	4.41E−15	2.93E−15	2.25E−14	1.44E−14	8.41E−15
8.0	1.81E−14	1.04E−14	8.56E−15	3.24E−15	2.14E−15	1.65E−14	1.05E−14	6.13E−15
8.1	1.34E−14	7.59E−15	6.24E−15	2.36E−15	1.55E−15	1.20E−14	7.67E−15	4.45E−15
8.2	9.89E−15	5.53E−15	4.53E−15	1.71E−15	1.12E−15	8.72E−15	5.55E−15	3.21E−15
8.3	7.27E−15	4.02E−15	3.28E−15	1.24E−15	8.04E−16	6.31E−15	4.01E−15	2.31E−15
8.4	5.33E−15	2.91E−15	2.37E−15	8.95E−16	5.76E−16	4.56E−15	2.88E−15	1.65E−15
8.5	3.90E−15	2.10E−15	1.71E−15	6.45E−16	4.12E−16	3.28E−15	2.07E−15	1.18E−15
8.6	2.85E−15	1.52E−15	1.23E−15	4.63E−16	2.94E−16	2.36E−15	1.48E−15	8.44E−16
8.7	2.08E−15	1.09E−15	8.82E−16	3.33E−16	2.10E−16	1.70E−15	1.06E−15	6.01E−16
8.8	1.51E−15	7.87E−16	6.33E−16	2.39E−16	1.50E−16	1.22E−15	7.59E−16	4.28E−16
8.9	1.10E−15	5.66E−16	4.54E−16	1.71E−16	1.06E−16	8.75E−16	5.42E−16	3.04E−16
9.0	7.99E−16	4.07E−16	3.26E−16	1.22E−16	7.57E−17	6.28E−16	3.87E−16	2.16E−16
				Mg X				
BE:	−27.0	−11.7	−25.6	−11.3	−11.1	−25.5	−11.3	−11.1
1.0	7.70E−11	2.44E−11	7.70E−11	2.83E−11	3.73E−11	1.53E−10	5.64E−11	5.58E−11
1.1	6.86E−11	2.18E−11	6.86E−11	2.52E−11	3.32E−11	1.36E−10	5.03E−11	4.97E−11
1.2	6.12E−11	1.94E−11	6.11E−11	2.25E−11	2.96E−11	1.22E−10	4.48E−11	4.43E−11
1.3	5.45E−11	1.73E−11	5.45E−11	2.00E−11	2.64E−11	1.08E−10	3.99E−11	3.95E−11
1.4	4.86E−11	1.54E−11	4.86E−11	1.78E−11	2.35E−11	9.66E−11	3.56E−11	3.52E−11
1.5	4.33E−11	1.37E−11	4.33E−11	1.59E−11	2.10E−11	8.61E−11	3.17E−11	3.14E−11
1.6	3.86E−11	1.22E−11	3.86E−11	1.42E−11	1.87E−11	7.67E−11	2.83E−11	2.80E−11
1.7	3.44E−11	1.09E−11	3.44E−11	1.26E−11	1.66E−11	6.84E−11	2.52E−11	2.49E−11
1.8	3.06E−11	9.72E−12	3.06E−11	1.13E−11	1.48E−11	6.09E−11	2.25E−11	2.22E−11
1.9	2.73E−11	8.67E−12	2.73E−11	1.00E−11	1.32E−11	5.43E−11	2.00E−11	1.98E−11
2.0	2.43E−11	7.72E−12	2.43E−11	8.94E−12	1.18E−11	4.84E−11	1.78E−11	1.76E−11
2.1	2.17E−11	6.88E−12	2.17E−11	7.97E−12	1.05E−11	4.31E−11	1.59E−11	1.57E−11
2.2	1.93E−11	6.14E−12	1.93E−11	7.10E−12	9.36E−12	3.84E−11	1.42E−11	1.40E−11
2.3	1.72E−11	5.47E−12	1.72E−11	6.33E−12	8.34E−12	3.43E−11	1.26E−11	1.25E−11
2.4	1.54E−11	4.87E−12	1.54E−11	5.64E−12	7.44E−12	3.05E−11	1.13E−11	1.11E−11
2.5	1.37E−11	4.34E−12	1.37E−11	5.03E−12	6.63E−12	2.72E−11	1.00E−11	9.92E−12
2.6	1.22E−11	3.87E−12	1.22E−11	4.48E−12	5.91E−12	2.43E−11	8.94E−12	8.84E−12
2.7	1.09E−11	3.45E−12	1.09E−11	3.99E−12	5.26E−12	2.16E−11	7.97E−12	7.88E−12
2.8	9.69E−12	3.08E−12	9.69E−12	3.56E−12	4.69E−12	1.93E−11	7.10E−12	7.02E−12
2.9	8.64E−12	2.74E−12	8.63E−12	3.17E−12	4.18E−12	1.72E−11	6.33E−12	6.26E−12
3.0	7.70E−12	2.44E−12	7.69E−12	2.83E−12	3.72E−12	1.53E−11	5.64E−12	5.58E−12
3.1	6.86E−12	2.18E−12	6.86E−12	2.52E−12	3.32E−12	1.36E−11	5.03E−12	4.97E−12
3.2	6.12E−12	1.94E−12	6.11E−12	2.24E−12	2.96E−12	1.22E−11	4.48E−12	4.43E−12
3.3	5.45E−12	1.73E−12	5.45E−12	2.00E−12	2.63E−12	1.08E−11	3.99E−12	3.94E−12
3.4	4.86E−12	1.54E−12	4.85E−12	1.78E−12	2.35E−12	9.65E−12	3.56E−12	3.51E−12
3.5	4.33E−12	1.37E−12	4.32E−12	1.59E−12	2.09E−12	8.60E−12	3.17E−12	3.13E−12
3.6	3.86E−12	1.22E−12	3.85E−12	1.42E−12	1.86E−12	7.66E−12	2.83E−12	2.79E−12
3.7	3.44E−12	1.09E−12	3.43E−12	1.26E−12	1.66E−12	6.83E−12	2.52E−12	2.48E−12
3.8	3.07E−12	9.73E−13	3.06E−12	1.12E−12	1.48E−12	6.08E−12	2.24E−12	2.21E−12
3.9	2.73E−12	8.67E−13	2.73E−12	1.00E−12	1.31E−12	5.42E−12	2.00E−12	1.97E−12
4.0	2.44E−12	7.73E−13	2.43E−12	8.92E−13	1.17E−12	4.83E−12	1.78E−12	1.75E−12
4.1	2.17E−12	6.89E−13	2.16E−12	7.95E−13	1.04E−12	4.30E−12	1.59E−12	1.56E−12
4.2	1.93E−12	6.14E−13	1.93E−12	7.08E−13	9.24E−13	3.83E−12	1.41E−12	1.38E−12
4.3	1.72E−12	5.47E−13	1.71E−12	6.30E−13	8.21E−13	3.41E−12	1.26E−12	1.23E−12
4.4	1.54E−12	4.88E−13	1.53E−12	5.61E−13	7.29E−13	3.04E−12	1.12E−12	1.09E−12
4.5	1.37E−12	4.35E−13	1.36E−12	4.99E−13	6.46E−13	2.70E−12	9.96E−13	9.67E−13
4.6	1.22E−12	3.88E−13	1.21E−12	4.44E−13	5.72E−13	2.40E−12	8.86E−13	8.57E−13
4.7	1.09E−12	3.46E−13	1.07E−12	3.95E−13	5.06E−13	2.14E−12	7.88E−13	7.58E−13

TABLE 4—*Continued*

log T (K)	α_R (cm^3 s^{-1})							
	$2s\ ^2S_{1/2}$	$3s\ ^2S_{1/2}$	$2p\ ^2P^o_{1/2}$	$3p\ ^2P^o_{1/2}$	$3d\ ^2D_{3/2}$	$2p\ ^2P^o_{3/2}$	$3p\ ^2P^o_{3/2}$	$3d\ ^2D_{5/2}$
				Mg x				
4.8	9.71E−13	3.09E−13	9.54E−13	3.51E−13	4.47E−13	1.90E−12	7.01E−13	6.69E−13
4.9	8.66E−13	2.75E−13	8.47E−13	3.12E−13	3.93E−13	1.69E−12	6.22E−13	5.89E−13
5.0	7.72E−13	2.45E−13	7.52E−13	2.77E−13	3.45E−13	1.49E−12	5.52E−13	5.17E−13
5.1	6.88E−13	2.19E−13	6.66E−13	2.45E−13	3.02E−13	1.32E−12	4.89E−13	4.52E−13
5.2	6.14E−13	1.95E−13	5.89E−13	2.17E−13	2.63E−13	1.17E−12	4.33E−13	3.94E−13
5.3	5.48E−13	1.74E−13	5.20E−13	1.92E−13	2.29E−13	1.03E−12	3.83E−13	3.42E−13
5.4	4.89E−13	1.56E−13	4.59E−13	1.69E−13	1.97E−13	9.12E−13	3.37E−13	2.95E−13
5.5	4.36E−13	1.39E−13	4.03E−13	1.49E−13	1.69E−13	8.01E−13	2.97E−13	2.53E−13
5.6	3.89E−13	1.24E−13	3.53E−13	1.30E−13	1.44E−13	7.02E−13	2.60E−13	2.16E−13
5.7	3.48E−13	1.11E−13	3.09E−13	1.14E−13	1.22E−13	6.13E−13	2.27E−13	1.83E−13
5.8	3.10E−13	9.86E−14	2.68E−13	9.92E−14	1.02E−13	5.33E−13	1.98E−13	1.53E−13
5.9	2.77E−13	8.79E−14	2.32E−13	8.59E−14	8.51E−14	4.62E−13	1.71E−13	1.27E−13
6.0	2.47E−13	7.83E−14	2.00E−13	7.39E−14	7.01E−14	3.97E−13	1.47E−13	1.05E−13
6.1	2.21E−13	6.98E−14	1.72E−13	6.33E−14	5.71E−14	3.41E−13	1.26E−13	8.56E−14
6.2	2.00E−13	6.25E−14	1.49E−13	5.42E−14	4.63E−14	2.95E−13	1.07E−13	7.02E−14
6.3	1.86E−13	5.78E−14	1.35E−13	4.74E−14	3.78E−14	2.64E−13	9.22E−14	6.07E−14
6.4	1.81E−13	5.73E−14	1.34E−13	4.41E−14	3.22E−14	2.55E−13	8.13E−14	6.04E−14
6.5	1.85E−13	6.23E−14	1.46E−13	4.51E−14	2.98E−14	2.67E−13	7.56E−14	7.15E−14
6.6	1.93E−13	7.16E−14	1.67E−13	4.97E−14	3.00E−14	2.93E−13	7.42E−14	9.19E−14
6.7	2.00E−13	8.20E−14	1.89E−13	5.57E−14	3.15E−14	3.20E−13	7.50E−14	1.16E−13
6.8	2.00E−13	9.00E−14	2.03E−13	6.04E−14	3.29E−14	3.36E−13	7.54E−14	1.35E−13
6.9	1.92E−13	9.29E−14	2.06E−13	6.19E−14	3.30E−14	3.34E−13	7.35E−14	1.45E−13
7.0	1.76E−13	9.01E−14	1.96E−13	5.98E−14	3.15E−14	3.14E−13	6.86E−14	1.44E−13
7.1	1.56E−13	8.28E−14	1.77E−13	5.46E−14	2.86E−14	2.81E−13	6.14E−14	1.34E−13
7.2	1.33E−13	7.25E−14	1.53E−13	4.76E−14	2.48E−14	2.41E−13	5.28E−14	1.18E−13
7.3	1.10E−13	6.11E−14	1.27E−13	3.99E−14	2.07E−14	2.00E−13	4.38E−14	9.99E−14
7.4	8.88E−14	4.99E−14	1.02E−13	3.24E−14	1.67E−14	1.60E−13	3.54E−14	8.13E−14
7.5	7.04E−14	3.97E−14	8.03E−14	2.56E−14	1.31E−14	1.26E−13	2.79E−14	6.44E−14
7.6	5.50E−14	3.10E−14	6.18E−14	1.98E−14	1.01E−14	9.68E−14	2.15E−14	4.98E−14
7.7	4.24E−14	2.37E−14	4.69E−14	1.51E−14	7.68E−15	7.34E−14	1.64E−14	3.79E−14
7.8	3.23E−14	1.80E−14	3.51E−14	1.13E−14	5.74E−15	5.49E−14	1.23E−14	2.84E−14
7.9	2.45E−14	1.35E−14	2.60E−14	8.39E−15	4.25E−15	4.07E−14	9.16E−15	2.10E−14
8.0	1.84E−14	1.00E−14	1.91E−14	6.18E−15	3.11E−15	3.00E−14	6.77E−15	1.54E−14
8.1	1.38E−14	7.40E−15	1.40E−14	4.52E−15	2.27E−15	2.19E−14	4.96E−15	1.12E−14
8.2	1.03E−14	5.44E−15	1.01E−14	3.29E−15	1.64E−15	1.59E−14	3.62E−15	8.13E−15
8.3	7.63E−15	3.98E−15	7.35E−15	2.38E−15	1.18E−15	1.15E−14	2.63E−15	5.86E−15
8.4	5.65E−15	2.90E−15	5.30E−15	1.72E−15	8.51E−16	8.34E−15	1.91E−15	4.21E−15
8.5	4.17E−15	2.11E−15	3.82E−15	1.24E−15	6.10E−16	6.01E−15	1.38E−15	3.01E−15
8.6	3.08E−15	1.53E−15	2.74E−15	8.89E−16	4.36E−16	4.32E−15	9.96E−16	2.15E−15
8.7	2.26E−15	1.11E−15	1.97E−15	6.37E−16	3.11E−16	3.11E−15	7.17E−16	1.54E−15
8.8	1.66E−15	8.05E−16	1.41E−15	4.56E−16	2.22E−16	2.23E−15	5.16E−16	1.09E−15
8.9	1.22E−15	5.82E−16	1.01E−15	3.27E−16	1.58E−16	1.60E−15	3.71E−16	7.79E−16
9.0	8.91E−16	4.20E−16	7.20E−16	2.33E−16	1.12E−16	1.14E−15	2.66E−16	5.53E−16

NOTES.—"BE" is the binding energy of the level in rydberg. Table 4 is also available in machine-readable form in the electronic edition of the *Astrophysical Journal Supplement*.

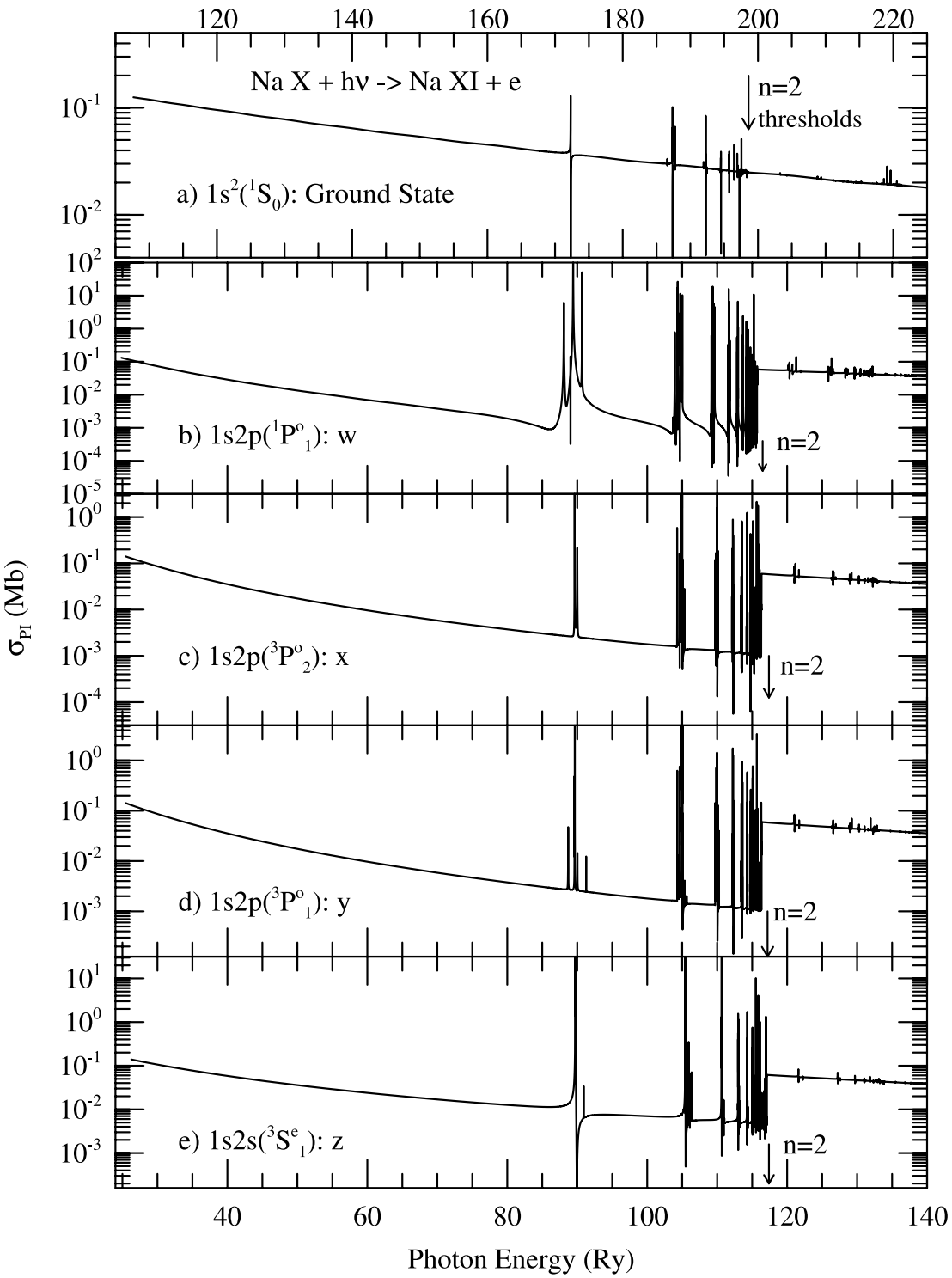

FIG. 7.—Level-specific photoionization cross sections of Na X: (*a*) the ground level, $1s^2(^1S_0)$, and four excited (*b*) $1s2p(^1P^o_1)$, (*c*) $1s2p(^3P^o_2)$, (*d*) $1s2p(^3P^o_1)$, and (*e*) $1s2s(^3S_1)$ levels corresponding to the prominent resonance (*w*), intercombination (*y*), and forbidden (*x*, *z*) diagnostic X-ray lines. K-shell ionization edge is noticed at the $n = 2$ thresholds for the excited levels.

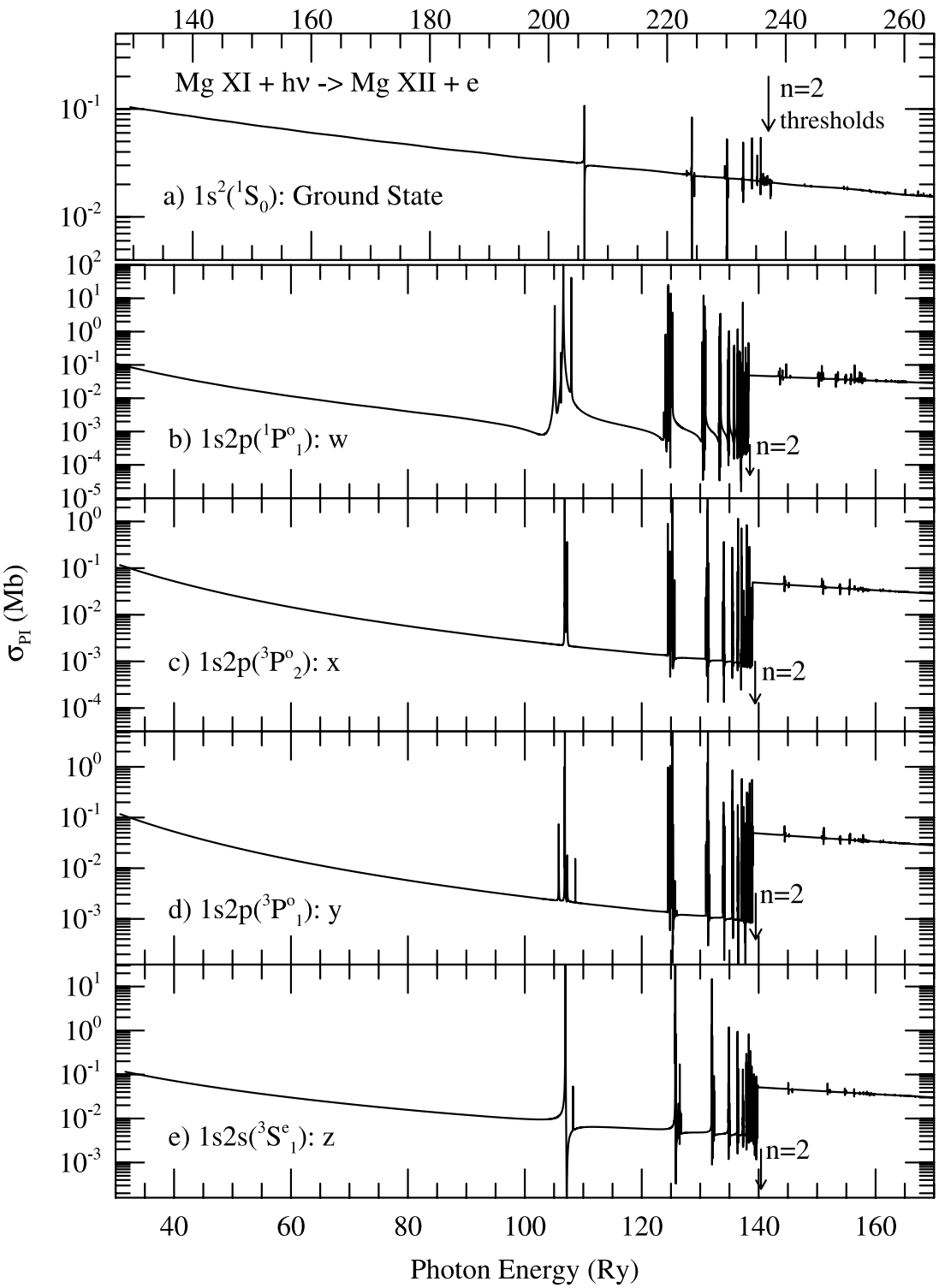

FIG. 8.—Level-specific photoionization cross sections of Mg XI: (*a*) the ground level, $1s^2(^1S_0)$, and four excited (*b*) $1s2p(^1P^o_1)$, (*c*) $1s2p(^3P^o_2)$, (*d*) $1s2p(^3P^o_1)$, and (*e*) $1s2s(^3S_1)$ levels corresponding to the prominent resonance (*w*), intercombination (*y*), and forbidden (*x*, *z*) diagnostic X-ray lines. K-shell ionization edge is noticed at the $n = 2$ thresholds for the excited levels.

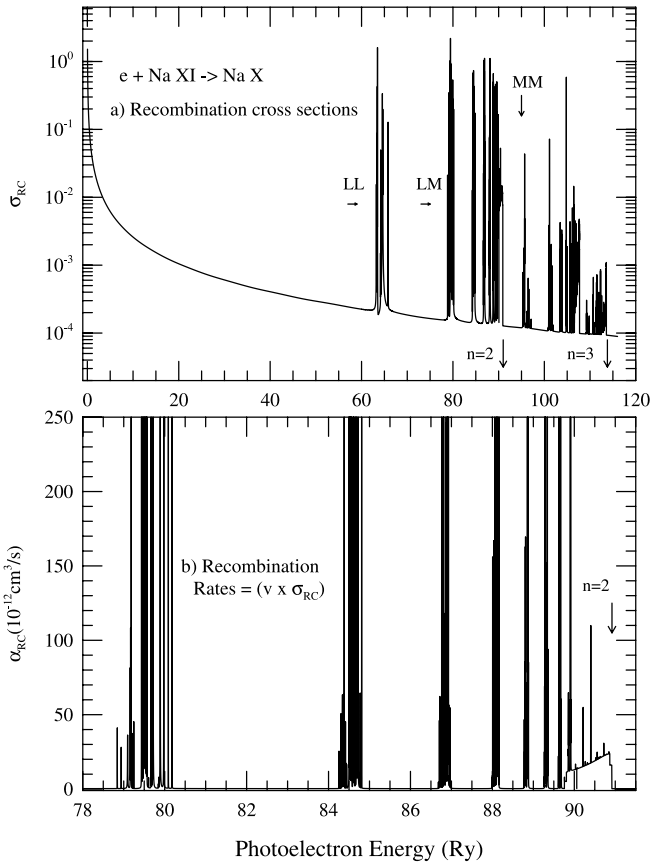

FIG. 9.—(*a*) Total unified (e + ion) recombination cross sections, σ_{RC} and (*b*) velocity dependent unified recombination rate coefficients, $\alpha_{RC}(E)$ for (e+ Na XI → Na X). Note the separated resonance complexes, LL, LM, etc., of $n = 2$ and MM, MN, etc., of $n = 3$ thresholds. The quantity $\alpha_{RC}(E)$, convolved with an energy bandwidth, is measurable.

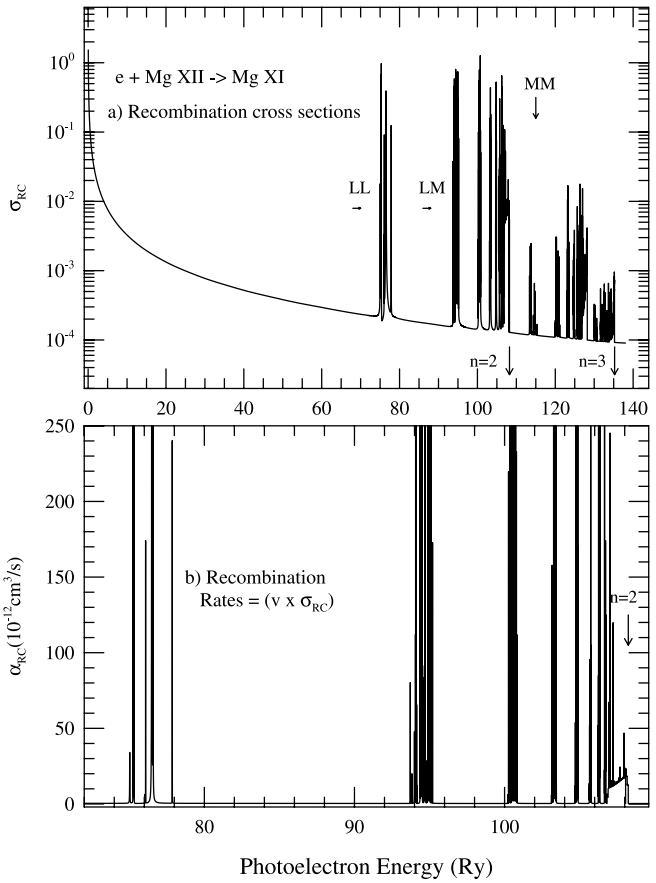

FIG. 10.—(*a*) Total unified (e + ion) recombination cross sections, σ_{RC} and (*b*) velocity dependent unified recombination rate coefficients, $\alpha_{RC}(E)$ for (e+ Mg XII → Mg XI). Note the separated resonance complexes, LL, LM, etc., of $n = 2$ and MM, MN, etc., of $n = 3$ thresholds. The quantity $\alpha_{RC}(E)$, convolved with an energy bandwidth, is measurable.

zero photoelectron energy σ_{RC} diverges (eq. [8]) but decays smoothly with energy until resonance complexes appear at very high energies. The Rydberg series of resonances form LL, LM, etc., complexes that converge on to the $n = 2$ thresholds, and MM, MN, etc., complexes that converge on to the $n = 3$ thresholds. LL denotes $2l2l'$, LM denotes $2l3l'$, etc. Some of the complexes are marked in the figures. The resonances become much weaker and narrower beyond $n = 2$ thresholds.

The velocity dependent photorecombination rates $\alpha_{RC}(E)$ for Na X and Mg XI are obtained for energies up to $n = 4$ thresholds of the respective core ions. However, resonances of $n = 2$ thresholds are stronger and hence are likely to be seen in experiments. $\alpha_{RC}(E)$ for Na X and Mg XI are shown in the bottom panels of Figures 9 and 10. The features of recombination rate, convolved with the experimental bandwidth, are observable in experiments.

Total unified recombination rate coefficients for Na X and Mg XI are presented for a wide range of temperature, $1 \leq \log T \leq 9$ tabulated in Table 3. The features are illustrated and compared with the available rates in Figures 11*a* and 11*b*. The BPRM unified $\alpha_R(T)$ (*solid curves*) show basic features. Starting high at very low temperatures due to the dominance of RR into an infinite number of high-n levels, the recombination rate coefficient decreases with increasing temperature until at high T, where it forms a "bump" due to dominant DR process, and follows to a smooth decay due to damping of recombination cross sections by the exponential of the Maxwellian electron distribution.

The present total unified recombination rate coefficients, $\alpha_R(T)$, for Na X and Mg XI compare very well with the RR rate

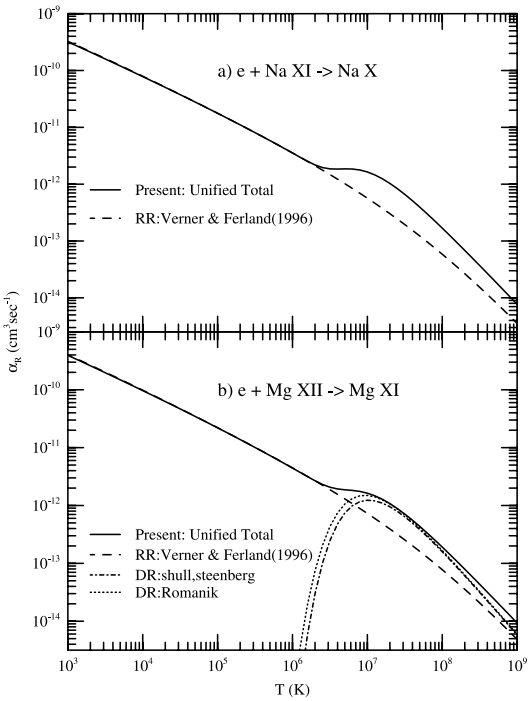

FIG. 11.—Total unified recombination rate coefficients $\alpha_R(T)$ (*solid curves*) for (*a*) Na X and (*b*) Mg XI. The RR rates are by Verner & Ferland (1996, *dashed line*). The DR rates are by Romanik (1988) (*dotted line*) and by Shull & van Steenberg (1982, *dot-dashed line*).

TABLE 5

LEVEL SPECIFIC RECOMBINATION RATE COEFFICIENTS FOR THE GROUND AND Kα LEVELS OF Na X AND Mg XI

log T (K)	α_R (cm^3 s^{-1})				
	$1s^2\ ^1S_0$	$1s2s\ ^3S_1$	$1s2p\ ^3P_1^o$	$1s2p\ ^1P_1^o$	$1s2p\ ^3P_2^o$
	Na X				
BE:	−108.	−26.3	−25.5	−24.9	−25.4
1.0	3.00E−10	5.94E−11	5.70E−11	5.05E−11	9.46E−11
1.1	2.67E−10	5.30E−11	5.08E−11	4.50E−11	8.43E−11
1.2	2.38E−10	4.72E−11	4.53E−11	4.01E−11	7.51E−11
1.3	2.12E−10	4.21E−11	4.03E−11	3.57E−11	6.70E−11
1.4	1.89E−10	3.75E−11	3.60E−11	3.18E−11	5.97E−11
1.5	1.69E−10	3.34E−11	3.20E−11	2.84E−11	5.32E−11
1.6	1.50E−10	2.98E−11	2.86E−11	2.53E−11	4.74E−11
1.7	1.34E−10	2.65E−11	2.55E−11	2.25E−11	4.22E−11
1.8	1.19E−10	2.37E−11	2.27E−11	2.01E−11	3.77E−11
1.9	1.06E−10	2.11E−11	2.02E−11	1.79E−11	3.36E−11
2.0	9.49E−11	1.88E−11	1.80E−11	1.60E−11	2.99E−11
2.1	8.46E−11	1.67E−11	1.61E−11	1.42E−11	2.67E−11
2.2	7.54E−11	1.49E−11	1.43E−11	1.27E−11	2.38E−11
2.3	6.72E−11	1.33E−11	1.28E−11	1.13E−11	2.12E−11
2.4	5.99E−11	1.19E−11	1.14E−11	1.01E−11	1.89E−11
2.5	5.34E−11	1.06E−11	1.01E−11	8.97E−12	1.68E−11
2.6	4.76E−11	9.42E−12	9.03E−12	8.00E−12	1.50E−11
2.7	4.24E−11	8.39E−12	8.05E−12	7.13E−12	1.34E−11
2.8	3.78E−11	7.48E−12	7.17E−12	6.35E−12	1.19E−11
2.9	3.37E−11	6.67E−12	6.39E−12	5.66E−12	1.06E−11
3.0	3.00E−11	5.94E−12	5.70E−12	5.05E−12	9.46E−12
3.1	2.67E−11	5.30E−12	5.08E−12	4.50E−12	8.43E−12
3.2	2.38E−11	4.72E−12	4.53E−12	4.01E−12	7.51E−12
3.3	2.12E−11	4.21E−12	4.03E−12	3.57E−12	6.69E−12
3.4	1.89E−11	3.75E−12	3.59E−12	3.18E−12	5.96E−12
3.5	1.69E−11	3.34E−12	3.20E−12	2.84E−12	5.31E−12
3.6	1.50E−11	2.98E−12	2.85E−12	2.53E−12	4.74E−12
3.7	1.34E−11	2.65E−12	2.54E−12	2.25E−12	4.22E−12
3.8	1.19E−11	2.37E−12	2.27E−12	2.01E−12	3.76E−12
3.9	1.06E−11	2.11E−12	2.02E−12	1.79E−12	3.35E−12
4.0	9.49E−12	1.88E−12	1.80E−12	1.59E−12	2.98E−12
4.1	8.46E−12	1.67E−12	1.60E−12	1.42E−12	2.66E−12
4.2	7.54E−12	1.49E−12	1.43E−12	1.26E−12	2.37E−12
4.3	6.71E−12	1.33E−12	1.27E−12	1.12E−12	2.11E−12
4.4	5.98E−12	1.19E−12	1.13E−12	1.00E−12	1.88E−12
4.5	5.33E−12	1.06E−12	1.01E−12	8.90E−13	1.67E−12
4.6	4.75E−12	9.42E−13	8.95E−13	7.91E−13	1.48E−12
4.7	4.23E−12	8.39E−13	7.95E−13	7.03E−13	1.32E−12
4.8	3.77E−12	7.48E−13	7.07E−13	6.25E−13	1.17E−12
4.9	3.36E−12	6.67E−13	6.27E−13	5.54E−13	1.04E−12
5.0	2.99E−12	5.94E−13	5.56E−13	4.91E−13	9.23E−13
5.1	2.67E−12	5.30E−13	4.93E−13	4.35E−13	8.18E−13
5.2	2.37E−12	4.72E−13	4.36E−13	3.85E−13	7.24E−13
5.3	2.11E−12	4.21E−13	3.85E−13	3.39E−13	6.39E−13
5.4	1.88E−12	3.75E−13	3.39E−13	2.98E−13	5.63E−13
5.5	1.67E−12	3.34E−13	2.98E−13	2.62E−13	4.95E−13
5.6	1.49E−12	2.97E−13	2.61E−13	2.29E−13	4.34E−13
5.7	1.32E−12	2.65E−13	2.28E−13	1.99E−13	3.79E−13
5.8	1.17E−12	2.36E−13	1.98E−13	1.73E−13	3.29E−13
5.9	1.04E−12	2.09E−13	1.72E−13	1.49E−13	2.85E−13
6.0	9.23E−13	1.86E−13	1.48E−13	1.28E−13	2.45E−13
6.1	8.17E−13	1.67E−13	1.26E−13	1.10E−13	2.10E−13
6.2	7.21E−13	1.52E−13	1.07E−13	9.92E−14	1.78E−13
6.3	6.36E−13	1.44E−13	9.09E−14	9.73E−14	1.51E−13
6.4	5.59E−13	1.44E−13	7.68E−14	1.06E−13	1.29E−13
6.5	4.90E−13	1.49E−13	6.49E−14	1.23E−13	1.10E−13
6.6	4.28E−13	1.55E−13	5.51E−14	1.41E−13	9.50E−14
6.7	3.72E−13	1.57E−13	4.67E−14	1.55E−13	8.24E−14
6.8	3.22E−13	1.53E−13	3.95E−14	1.59E−13	7.11E−14
6.9	2.77E−13	1.43E−13	3.30E−14	1.53E−13	6.08E−14

TABLE 5—*Continued*

log T (K)	α_R (cm^3 s^{-1})				
	$1s^2\ ^1S_0$	$1s2s\ ^3S_1$	$1s2p\ ^3P^o_1$	$1s2p\ ^1P^o_1$	$1s2p\ ^3P^o_2$
			Na x		
7.0	2.37E−13	1.28E−13	2.73E−14	1.39E−13	5.12E−14
7.1	2.01E−13	1.10E−13	2.23E−14	1.21E−13	4.23E−14
7.2	1.69E−13	9.23E−14	1.79E−14	1.01E−13	3.43E−14
7.3	1.41E−13	7.53E−14	1.42E−14	8.17E−14	2.73E−14
7.4	1.17E−13	6.01E−14	1.11E−14	6.44E−14	2.15E−14
7.5	9.62E−14	4.72E−14	8.59E−15	4.97E−14	1.66E−14
7.6	7.85E−14	3.65E−14	6.59E−15	3.78E−14	1.27E−14
7.7	6.35E−14	2.80E−14	5.01E−15	2.83E−14	9.69E−15
7.8	5.10E−14	2.13E−14	3.79E−15	2.10E−14	7.31E−15
7.9	4.06E−14	1.60E−14	2.85E−15	1.55E−14	5.48E−15
8.0	3.22E−14	1.20E−14	2.13E−15	1.13E−14	4.09E−15
8.1	2.53E−14	8.98E−15	1.59E−15	8.23E−15	3.04E−15
8.2	1.98E−14	6.68E−15	1.18E−15	5.96E−15	2.25E−15
8.3	1.54E−14	4.95E−15	8.76E−16	4.31E−15	1.66E−15
8.4	1.19E−14	3.66E−15	6.47E−16	3.10E−15	1.22E−15
8.5	9.15E−15	2.70E−15	4.78E−16	2.23E−15	8.98E−16
8.6	7.01E−15	1.99E−15	3.52E−16	1.60E−15	6.59E−16
8.7	5.34E−15	1.46E−15	2.59E−16	1.15E−15	4.83E−16
8.8	4.06E−15	1.07E−15	1.90E−16	8.20E−16	3.53E−16
8.9	3.07E−15	7.85E−16	1.39E−16	5.86E−16	2.58E−16
9.0	2.32E−15	5.74E−16	1.02E−16	4.19E−16	1.88E−16
			Mg xi		
BE:	−129.	−31.7	−30.8	−30.1	−30.7
1.0	3.60E−10	7.17E−11	6.87E−11	6.14E−11	1.14E−10
1.1	3.21E−10	6.39E−11	6.12E−11	5.47E−11	1.01E−10
1.2	2.86E−10	5.70E−11	5.45E−11	4.87E−11	9.04E−11
1.3	2.55E−10	5.08E−11	4.86E−11	4.34E−11	8.06E−11
1.4	2.27E−10	4.52E−11	4.33E−11	3.87E−11	7.18E−11
1.5	2.02E−10	4.03E−11	3.86E−11	3.45E−11	6.40E−11
1.6	1.80E−10	3.59E−11	3.44E−11	3.08E−11	5.70E−11
1.7	1.61E−10	3.20E−11	3.07E−11	2.74E−11	5.08E−11
1.8	1.43E−10	2.85E−11	2.73E−11	2.44E−11	4.53E−11
1.9	1.28E−10	2.54E−11	2.44E−11	2.18E−11	4.04E−11
2.0	1.14E−10	2.27E−11	2.17E−11	1.94E−11	3.60E−11
2.1	1.01E−10	2.02E−11	1.93E−11	1.73E−11	3.21E−11
2.2	9.04E−11	1.80E−11	1.72E−11	1.54E−11	2.86E−11
2.3	8.06E−11	1.61E−11	1.54E−11	1.37E−11	2.55E−11
2.4	7.18E−11	1.43E−11	1.37E−11	1.22E−11	2.27E−11
2.5	6.40E−11	1.28E−11	1.22E−11	1.09E−11	2.02E−11
2.6	5.70E−11	1.14E−11	1.09E−11	9.72E−12	1.80E−11
2.7	5.08E−11	1.01E−11	9.70E−12	8.67E−12	1.61E−11
2.8	4.53E−11	9.03E−12	8.64E−12	7.72E−12	1.43E−11
2.9	4.04E−11	8.05E−12	7.70E−12	6.88E−12	1.28E−11
3.0	3.60E−11	7.17E−12	6.86E−12	6.13E−12	1.14E−11
3.1	3.21E−11	6.39E−12	6.12E−12	5.47E−12	1.01E−11
3.2	2.86E−11	5.70E−12	5.45E−12	4.87E−12	9.04E−12
3.3	2.55E−11	5.08E−12	4.86E−12	4.34E−12	8.05E−12
3.4	2.27E−11	4.53E−12	4.33E−12	3.87E−12	7.18E−12
3.5	2.02E−11	4.03E−12	3.86E−12	3.45E−12	6.39E−12
3.6	1.80E−11	3.59E−12	3.44E−12	3.07E−12	5.70E−12
3.7	1.61E−11	3.20E−12	3.06E−12	2.74E−12	5.08E−12
3.8	1.43E−11	2.86E−12	2.73E−12	2.44E−12	4.52E−12
3.9	1.28E−11	2.55E−12	2.43E−12	2.17E−12	4.03E−12
4.0	1.14E−11	2.27E−12	2.17E−12	1.94E−12	3.59E−12
4.1	1.01E−11	2.02E−12	1.93E−12	1.72E−12	3.20E−12
4.2	9.03E−12	1.80E−12	1.72E−12	1.54E−12	2.85E−12
4.3	8.05E−12	1.61E−12	1.53E−12	1.37E−12	2.54E−12
4.4	7.17E−12	1.43E−12	1.36E−12	1.22E−12	2.26E−12
4.5	6.39E−12	1.28E−12	1.21E−12	1.08E−12	2.01E−12
4.6	5.70E−12	1.14E−12	1.08E−12	9.63E−13	1.79E−12
4.7	5.07E−12	1.01E−12	9.60E−13	8.56E−13	1.59E−12

TABLE 5—*Continued*

log T (K)	α_R (cm^3 s^{-1})				
	$1s^2\ ^1S_0$	$1s2s\ ^3S_1$	$1s2p\ ^3P^o_1$	$1s2p\ ^1P^o_1$	$1s2p\ ^3P^o_2$
	Mg XI				
4.8	4.52E−12	9.03E−13	8.53E−13	7.61E−13	1.41E−12
4.9	4.03E−12	8.05E−13	7.58E−13	6.76E−13	1.26E−12
5.0	3.59E−12	7.17E−13	6.73E−13	5.99E−13	1.11E−12
5.1	3.19E−12	6.39E−13	5.96E−13	5.31E−13	9.89E−13
5.2	2.84E−12	5.70E−13	5.28E−13	4.70E−13	8.75E−13
5.3	2.53E−12	5.08E−13	4.67E−13	4.15E−13	7.74E−13
5.4	2.25E−12	4.52E−13	4.12E−13	3.66E−13	6.83E−13
5.5	2.00E−12	4.03E−13	3.63E−13	3.22E−13	6.02E−13
5.6	1.78E−12	3.59E−13	3.19E−13	2.82E−13	5.29E−13
5.7	1.59E−12	3.20E−13	2.79E−13	2.47E−13	4.63E−13
5.8	1.41E−12	2.84E−13	2.44E−13	2.15E−13	4.04E−13
5.9	1.25E−12	2.53E−13	2.12E−13	1.86E−13	3.51E−13
6.0	1.11E−12	2.25E−13	1.83E−13	1.60E−13	3.03E−13
6.1	9.82E−13	2.00E−13	1.57E−13	1.38E−13	2.60E−13
6.2	8.68E−13	1.79E−13	1.34E−13	1.20E−13	2.23E−13
6.3	7.66E−13	1.63E−13	1.14E−13	1.09E−13	1.89E−13
6.4	6.75E−13	1.54E−13	9.64E−14	1.10E−13	1.61E−13
6.5	5.93E−13	1.52E−13	8.13E−14	1.21E−13	1.37E−13
6.6	5.19E−13	1.55E−13	6.84E−14	1.40E−13	1.18E−13
6.7	4.53E−13	1.57E−13	5.75E−14	1.58E−13	1.02E−13
6.8	3.93E−13	1.55E−13	4.82E−14	1.69E−13	8.81E−14
6.9	3.40E−13	1.49E−13	4.01E−14	1.70E−13	7.57E−14
7.0	2.92E−13	1.36E−13	3.31E−14	1.60E−13	6.43E−14
7.1	2.49E−13	1.21E−13	2.69E−14	1.44E−13	5.37E−14
7.2	2.11E−13	1.03E−13	2.17E−14	1.23E−13	4.40E−14
7.3	1.77E−13	8.57E−14	1.72E−14	1.02E−13	3.54E−14
7.4	1.48E−13	6.96E−14	1.35E−14	8.18E−14	2.81E−14
7.5	1.22E−13	5.54E−14	1.05E−14	6.41E−14	2.19E−14
7.6	1.00E−13	4.35E−14	8.12E−15	4.92E−14	1.69E−14
7.7	8.16E−14	3.37E−14	6.22E−15	3.73E−14	1.30E−14
7.8	6.59E−14	2.58E−14	4.73E−15	2.79E−14	9.82E−15
7.9	5.29E−14	1.96E−14	3.57E−15	2.06E−14	7.40E−15
8.0	4.21E−14	1.48E−14	2.69E−15	1.52E−14	5.54E−15
8.1	3.33E−14	1.12E−14	2.01E−15	1.11E−14	4.13E−15
8.2	2.61E−14	8.35E−15	1.51E−15	8.04E−15	3.07E−15
8.3	2.04E−14	6.22E−15	1.12E−15	5.82E−15	2.27E−15
8.4	1.58E−14	4.63E−15	8.33E−16	4.20E−15	1.68E−15
8.5	1.22E−14	3.43E−15	6.17E−16	3.03E−15	1.24E−15
8.6	9.41E−15	2.54E−15	4.56E−16	2.17E−15	9.08E−16
8.7	7.20E−15	1.87E−15	3.37E−16	1.56E−15	6.67E−16
8.8	5.49E−15	1.38E−15	2.48E−16	1.12E−15	4.89E−16
8.9	4.16E−15	1.01E−15	1.83E−16	8.01E−16	3.58E−16
9.0	3.15E−15	7.44E−16	1.34E−16	5.73E−16	2.61E−16

NOTES.—"BE" is the binding energy of the level in rydberg. Table 4 is also available in machine-readable form in the electronic edition of the *Astrophysical Journal Supplement*.

coefficients by Verner & Ferland (1996, *dashed line*) until the rise due to DR dominance, which they do not consider. The high-temperature peak of the present rate agrees very well with those by Romanik (1988, *dot-dashed line*). The fit to DR rates by Shull & van Steenberg (1982, *dot-dashed line*; values are fitted from the works of Jacobs et al. as referenced in their papers) is somewhat lower at the peak for Mg XI. There is no DR rate for Na X available for comparison.

Level-specific recombination rate coefficients for all 182 levels of Na X and 185 levels of Mg XI are obtained and are available electronically. They correspond to n (SLJ) with $0 \leq J \leq 10$ and $n \leq 10$. Table 5 presents level specific recombination rates for the ground level and excited $n = 2$ levels corresponding to the X-ray w, x, y, and z lines of Na X and Mg XI. The rates show a relatively smooth decay with temperature and a small shoulder at high temperatures due to DR resonances.

5. CONCLUSION

Extensive sets of self-consistent results are presented from detailed study of the photoionization and electron-ion recombination for Na IX, Na X, Mg X, and Mg XI using the unified method for the total recombination. Calculations include relativistic effects in the Breit-Pauli ***R***-matrix method. Level-specific photoionization and recombination cross sections and rate coefficients for all fine-structure levels up to $n \leq 10$ for Li-like Na IX, and Mg X and He-like Na X and Mg XI are obtained for the first time. Total recombination rates for the hydrogenic ions Na XI and Mg XII are also presented. The calculated energies are in very good

agreement with the measured values. The unified total recombination rate coefficients agree very well with the existing RR and DR rates by others. The present atomic data are expected to be of high accuracy based on the very good agreement of the energies with the experimental values, inclusion of atomic effects such as relativistic effects, radiation damping of resonances, channel couplings, and accuracy of the method. The results are more than sufficient for extrapolation to high-n, ℓ necessary to account for all recombination cascade contributions. The results should be useful for UV and X-ray spectroscopy of laboratory and astrophysical sources.

With featureless hydrogenic behavior for a relatively large temperature range, the recombination rates of these few electron systems show isoelectronic z-dependency. Similar to the rate of a hydrogenic ion, which varies as $z\alpha_R(H, T/z^2)$, the rate increases with higher ionic charge. The resonances are not z-dependent, except they get narrower with higher charge. Hence, the z-dependent isoelectronic behavior is not at high temperatures where the DR starts contributing.

The complete set of data includes (1) photoionization cross sections, both total and partial, for all fine-structure levels of Na IX, Na X, Mg X, and Mg XI up to $n = 10$, (2) total unified recombination rate coefficients and level-specific recombination rate coefficients for levels up to $n = 10$ for a wide temperature range, and (3) total unified recombination cross sections and recombination rate coefficients as functions of the photoelectron energy for comparison with experiments.

All photoionization and recombination data are available electronically from the author.

This work was supported partially by the NASA Astrophysical Research and Analysis program. The computational work was carried out at the Ohio Supercomputer Center in Columbus, Ohio.

REFERENCES

Bell, R. H., & Seaton, M. J. 1985, J. Phys. B, 18, 1589
Berrington, K. A., Burke, P. G., Butler, K., Seaton, M. J., Storey, P. J., Taylor, K. T., & Yu Yan. 1987, J. Phys. B, 20, 6379
Berrington, K. A., Eissner, W., & Norrington, P. H. 1995, Comput. Phys. Commun., 92, 290
Eissner, W., Jones, M., & Nussbaumer, H. 1974, Comput. Phys. Commun., 8, 270
Hillier, J. 2005, *Chandra* Proposal 07200982
Hummer, D. G., Berrington, K. A., Eissner, W., Pradhan, A. K., Saraph, H. E., & Tully, J. A. 1993, A&A, 279, 298
Nahar, S. N. 2002, A&A, 389, 716
———. 1996, Phys. Rev. A, 53, 2417
———. 2005, ApJS, 158, 80
———. 2006, ApJS, 164, 280
Nahar, S. N., & Pradhan, A. K. 1992, Phys. Rev. Lett., 68, 1488
———. 1994, Phys. Rev. A, 49, 1816
———. 1997, ApJS, 111, 339
———. 2000, Phys. Scr., 61, 675
Nahar, S. N., & Pradhan, A. K. 2003, ApJS, 149, 239
———. 2006a, ApJS, 162, 417
———. 2006b, Phys. Rev. A, 73, 062718
Nahar, S. N., Pradhan, A. K., & Zhang, H. L. 2000, ApJS, 131, 375
———. 2001, ApJS, 133, 255
Oelgoetz, J., & Pradhan, A. K. 2001, MNRAS, 327, L42
———. 2004, MNRAS, 354, 1093
Pradhan, A. K., Chen, G. X., Nahar, S. N., & Zhang, H. L. 2001, Phys. Rev. Lett., 87, 183201
Pradhan, A. K., & Zhang, H. L. 1997, J. Phys. B, 30, L571
Romanik, C. 1988, ApJ, 330, 1022
Sakimoto, K., Terao, M., & Berrington, K. A. 1990, Phys. Rev. A, 42, 291
Scott, N. S., & Burke, P. G. 1980, J. Phys. B, 12, 4299
Scott, N. S., & Taylor, K. T. 1982, Comput. Phys. Commun., 25, 347
Shull, J. M., & van Steenberg, M. 1982, ApJS, 48, 95
Verner, D. A., & Ferland, G. 1996, ApJS, 103, 467
Yan, Y., & Seaton, M. J. 1987, J. Phys. B, 20, 6409
Zhang, H. L., Nahar, S. N., & Pradhan, A. K. 1999, J. Phys. B, 32, 1459